Chemical Engineering & Processing: Process Intensification 228 (2026) 110960

Contents lists available at ScienceDirect

Chemical Engineering and Processing - Process Intensification

journal homepage: www.elsevier.com/locate/cep

Modeling and stability analysis of electrified reverse water–gas shift reactors

Giuseppe Andriani [a], Paolo Mocellin [a,c,*], Gianmaria Pio [b], Ernesto Salzano [b], Chiara Vianello [a]

[a] Dipartimento di Ingegneria Industriale – Università degli Studi di Padova, Via Marzolo 9, Padova, Italia
[b] Dipartimento di Ingegneria Civile, Chimica, Ambientale e dei Materiali – Università di Bologna, Via Terracini 28, Bologna, Italia
[c] Dipartimento di Ingegneria Civile, Edile e Ambientale – Università degli Studi di Padova, Via Marzolo 9, Padova, Italia

ARTICLE INFO

Keywords:
Chemical reaction engineering
Electrified reactors
Operability diagrams
Cold spots
Endothermic reactions

ABSTRACT

Loss-of-control and stability analyses of chemical reactors have traditionally focused on exothermic systems, whereas endothermic processes remain far less explored from a formal dynamical-systems perspective. Nevertheless, disturbances in operating conditions or failures in heat-supply units may also induce critical behaviour in endothermic reactors, including cold-spot formation and loss of operability.

In this work, the Varma–Morbidelli–Wu theory of parametric sensitivity analysis is adapted and applied to endothermic reactor systems, with specific focus on fixed-bed Joule-heated reactors. The proposed framework enables systematic identification of stability, operability, and performance limits through operability and performance diagrams expressed as two-dimensional parametric maps. These maps provide a priori tools for reactor design, control, and process intensification under electrified operation.

The reverse water–gas shift (rWGS) reaction is adopted as a representative case study due to its relevance in carbon capture and utilization. A thermodynamic assessment and comparative evaluation of literature kinetic models support the development of consistent one- and two-dimensional reactor models, which are used to perform parametric and sensitivity analyses with respect to design variables, operating conditions, and electrical heating intensity.

The analysis shows that cold-spot regimes emerge as structurally distinct steady-state operating regimes rather than as purely numerical artifacts. Intensified and high-performing operating windows are identified for both short- and long-contact-time configurations, clarifying the interplay between electrical current, reactor design, and operating conditions in defining operability limits. Moreover, the transition between regimes is governed by the competition between distributed Joule heating and cumulative endothermic heat absorption along the reactor length.

Overall, the proposed methodology provides an operability-oriented framework for the analysis of electrified endothermic reactors, supporting identification of operating regimes, operability margins, and performance–thermal trade-offs beyond the specific rWGS case study considered.

1. Introduction

Most studies on reactor loss of control have traditionally focused on exothermic systems, where thermal runaway represents one of the most critical industrial safety challenges [1]. Active and passive protection strategies are commonly adopted to mitigate these hazards by venting gaseous products and limiting over-pressurization [2]. However, the implementation of dedicated safety devices may be impractical in certain reactor configurations due to mechanical or process constraints [3]. Consequently, the integration of intrinsic safety principles into reactor design, control, and optimization has become increasingly important to ensure robust operation while balancing performance and sustainability requirements [4]. In this context, runaway behaviour can be interpreted as a manifestation of intrinsic system instability, which can be anticipated and avoided through appropriate modelling and stability-analysis tools.

Sensitivity analysis has long been employed to characterize the stability of exothermic reactors, enabling systematic identification of both unstable regimes (e.g., runaway) and stable operating states. A key outcome of this approach is the construction of stability and performance diagrams, which provide compact, two-dimensional

* Corresponding author.
E-mail address: paolo.mocellin@unipd.it (P. Mocellin).

https://doi.org/10.1016/j.cep.2026.110960
Received 9 February 2026; Received in revised form 30 May 2026; Accepted 12 July 2026
Available online 13 July 2026

Nomenclature

A lateral surface area of a tube
$a = \frac{150L(1-\varepsilon_{bed})^2}{P_{in}} \frac{\mu}{d_{cat}^2 \varepsilon_{bed}^3 v_{z,in}}$ First Ergun parameter
AE Algebraic equation
$B = \frac{\left(-\Delta\widetilde{H}_{r,f}\right)C_{CO_2,inlet}}{\rho_{mix}\widehat{C}_{p,mix}T_{inlet}}$ Dimensionless heat of reaction
$b = \frac{1.75L\rho}{P_{in}} \frac{(1-\varepsilon_{bed})}{d_{cat}} \frac{}{\varepsilon_{bed}^3 v_{z,in}^2}$ Second Ergun parameter
Bi Biot number
$\widetilde{C}_p$ Heat capacity per unit mole
$\widehat{C}_p$ Heat capacity per unit mass
CCU carbon capture and utilization
CCS carbon capture and storage
CSO First cold-spot region
CSO_2 Second cold-spot region
$\mathscr{D}$ Diffusivity
D Diameter
$Da = \frac{L_{tubes}\left|r'''_{rWGS}\left(T_{inlet},C_{CO_2,inlet}\right)\right|}{v_z C_{CO_2,inlet}}$ Damköhler number
ER Electrified reactor
h_T Heat transfer coefficient
$H_{r(b,f)} = \frac{-\Delta\widetilde{H}_{r,b}}{-\Delta\widetilde{H}_{r,f}}$ Dimensionless heat of reaction ratio
HTO High temperature operation
I_{tubes} Electrical current per single tube
$K_{C,eq}$ Equilibrium constant
k_T Thermal conductivity
L Length
MOL Method of lines
$\dot{n}$ molar flow rate per single tube
ODE Ordinary differential equation
P Dimensional pressure
$\mathscr{P} = \frac{P}{P_{in}}$ Dimensionless pressure
PAO pseudo-adiabatic operation region
PDE Partial differential equation
$Pe_{m,cat} = \frac{L_{tubes}v_z}{\mathscr{D}_{eff,i}}$ Catalyst mass Peclet number
$Pe_{m,r} = \frac{L_{tubes}v_z}{\mathscr{D}_{i,r}}$ Radial mass Peclet number
$Pe_T = \frac{\rho_{mix}\widehat{C}_{P,mix}L_{tubes}v_z}{k_{T,eff}}$ Thermal Peclet number
$\dot{Q}$ Thermal power exchanged
r Radial coordinate
$\varrho_{cat} = \frac{r_{cat}}{R_{cat}}$ Dimensionless catalyst radius
$R_f = \frac{r'''_f\left(T_{s,cat},C_{i,s,cat}\right)}{r'''_f\left(T_{inlet},C_{CO_2,inlet}\right)}$ Forward dimensionless reaction rate
$R_b = \frac{r'''_b\left(T_{s,cat},C_{i,s,cat}\right)}{r'''_b\left(T_{inlet},C_{CO_2,inlet}\right)}$ Backward dimensionless reaction rate
r' Dimensional reaction rate
R_{cat} Catalyst particle radius
$R^{in}_{r(b,f)} = \frac{r'''_b\left(T_{inlet},C_{CO_2,inlet}\right)}{r'''_f\left(T_{inlet},C_{CO_2,inlet}\right)}$ Dimensionless reaction rate ratio
RUN Runaway region
$rWGS$ reverse water gas shift
s Two times the thickness
$s(\Theta;B)$ Sensitivity of Θ with respect to B
$S(\Theta;B)$ Normalized sensitivity of Θ with respect to B
$SENS$ intrinsic sensitive region
$St = \frac{4UL_{tubes}}{D_{tubes}v_z\rho_{mix}\widehat{C}_{p,mix}}$ Stanton number
t Thickness
T Dimensional temperature
$u_i = \frac{C_i}{C_{CO_2,inlet}}$ Dimensionless concentration
V Reactor volume
v_z Superficial velocity
$\nu_z = \frac{v_z}{v_{z,in}}$ Dimensionless superficial velocity
$VMWT$ Varma, Morbidelli and Wu theory on parametric sensitivity analysis
y Molar fraction
$Yield_{out}$ Outlet yield
z Dimensional axial coordinate
$\varkappa = \frac{z}{L_{tubes}}$ Dimensionless axial coordinate
$\beta = \frac{D_{tubes}^2}{s_{tubes}(2D_{tubes}+s_{tubes})}$ Tube's wall aspect ratio
$\gamma = \frac{E_{a,f}}{R_g T_{inlet}}$ Dimensionless activation energy
$\Delta\widetilde{H}_r$ Reaction enthalpy
ε_{bed} Catalyst bed void fraction
$\zeta = \frac{k_{T,wall}}{k_{T,eff}}$ Thermal conductivity ratio
η Effectiveness factor
$\Theta = \frac{\gamma(T-T_{inlet})}{T_{inlet}}$ Dimensionless temperature
μ Viscosity
ν Stoichiometric coefficient
$\xi_i = \frac{k_{m,i}a_{cat}L_{tubes}}{v_z}$ Dimensionless mass transport coefficient
$\xi_T = \frac{h_T a_{cat} L_{tubes}}{\rho_{mix}\widehat{C}_{p,mix}v_z}$ Dimensionless heat transport coefficient
$\Xi_{cat} = \frac{R_{cat}}{D_{tubes}/2}$ Catalyst aspect ratio
$\Xi_{tubes} = \frac{L_{tubes}}{D_{tubes}/2}$ Tubes aspect ratio
ρ Density
ρ_{elett} Electrical resistivity
$\varphi_{cat} = \frac{\rho_{mix}\widehat{C}_{p,mix}}{\rho_{cat}\widehat{C}_{P,cat}}$ Catalyst dimensionless thermal inertia
$\varphi_{wall} = \frac{\rho_{mix}\widehat{C}_{p,mix}}{\rho_{wall}\widehat{C}_{P,wall}}$ Wall dimensionless thermal inertia
χ Conversion
$\mho = \frac{4}{L_{tubes}\pi D_{tubes}^2} \frac{\rho_{elett}I_{wall}^2}{\pi T_{inlet}v_z\rho_{wall}\widehat{C}_{P,wall}}$ Dimensionless Joule heating effect number

Subscripts and superscripts

$'''$ Value per unit volume
b Backward reaction
cat Catalyst's value
CO Value referred to CO
CO_2 Value referred to CO_2
eff Effective value
er Effective radial value
ex Exchanged value
f Forward reaction
gen Generated value
H_2 Value referred to H_2
H_2O Value referred to H_2O
i Value referred to i-th component
in Inlet value
$Knudsen$ Knudsen value
m Value referred to mass transport
min Minimum value
$molecular$ Molecular value
out Outlet value
$pore$ Pore value
r Value referred to a generic reaction
R Reactor's value
s Value referred to catalyst's surface
T Value referred to heat transport
$tube$ Value referred to a single tube
$wall$ Value referred to tube's wall

representations of reactor behaviour under varying operating conditions [5]. Classical frameworks, including the Varma–Morbidelli–Wu theory of parametric sensitivity analysis (VMWT) and related formulations by Westerterp et al. [6], explicitly promote the use of such maps as design-oriented tools to assess operability, safety margins, and performance trade-offs [7].

Although endothermic reactions are not susceptible to thermal runaway [8], they may still exhibit critical behaviour under process disturbances or auxiliary equipment failures [9]. Their performance is strongly constrained by heat-supply efficiency and temperature distribution, which directly affect conversion and selectivity [10]. Inadequate thermal management may lead to cold-spot formation, reducing process efficiency and potentially compromising operability [11]. Therefore, extending operability-oriented analysis tools to endothermic systems is essential to systematically address thermal-management-driven limitations at the design, control, and optimization stages, thereby supporting stable and sustainable operation of intensified endothermic processes [12]. Unlike exothermic systems, where thermal runaway and strong positive thermal feedback often govern reactor operability limits, endothermic reactors are primarily constrained by insufficient heat supply, temperature deficits, and cold-spot formation. Consequently, the physical interpretation of sensitivity branches and operating-regime transitions differs from that commonly encountered in exothermic reactor systems. In electrified endothermic reactors, fluctuations in electrical heating or inlet conditions may induce localized thermal deficits, performance deterioration, or loss of thermal operability rather than runaway behaviour. Accordingly, application of the VMWT framework to these systems requires reinterpretation of the resulting sensitivity patterns and operating-regime boundaries within an endothermic and electrically heated context.

From this perspective, the design, control, and optimization of endothermic reactors critically depend on effective thermal management [13]. Operability- and performance-oriented tools, such as sensitivity-based frameworks, can address these challenges already at the conceptual design stage by identifying process and design conditions that ensure reliable and robust operation under variable boundary conditions [14]. By delineating transitions between operating regimes, these methods help prevent intrinsically unsafe or non-performative behaviour. In this regard, operability and performance diagrams are particularly attractive, as they provide compact and intuitive representations of overall system behaviour under varying inputs.

These aspects are especially relevant in the context of sustainable and intensified endothermic processes [15], where reactor electrification is increasingly pursued as an alternative to combustion-based heat supply. Electrified reactors can reduce emissions and by-products [16,17], particularly when coupled with renewable electricity [18], while enabling more compact and intensified designs by eliminating external furnaces and heat-recovery units [19]. However, despite their growing interest, electrified reactor systems remain insufficiently understood in terms of operating regimes, response to fluctuating inputs, and intrinsic stability. This issue is further amplified by the intrinsically variable nature of electrified operation, where fluctuations in electrical input and feed conditions may directly affect reactor stability and operability. While existing studies mainly address performance and energy efficiency [20,21], the stability and operability of electrified endothermic reactors remain far less explored [22]. Indeed, existing analyses are generally limited to local parametric studies or reactor-specific simulations and do not provide generalized operability-oriented frameworks capable of identifying operating regimes, regime-transition boundaries, or operability margins under variable electrified operation. This gap motivates the need for a rigorous, operability-oriented framework capable of elucidating the fundamental behaviour and operability limits of electrified endothermic reactors.

In this context, the present work introduces a sensitivity-based methodology for the stability-oriented analysis and design of electrified endothermic reactors, which extends the application of classical parametric sensitivity frameworks, such as the VMWT, to electrified endothermic systems. This extension enables the construction of regimes and performance diagrams in which cold-spot regimes and operability limits emerge as structural features of the reactor dynamics rather than as purely numerical artifacts, supporting reactor design and control decisions. For clarity, the term "stability" is used here in the sense of steady-state parametric sensitivity and thermal operability within the classical VMWT framework, rather than linear dynamic stability assessed through transient eigenvalue analysis.

Among the various concepts proposed for electrified chemical reactors, Joule-heated multitubular fixed-bed systems represent one of the most mature and industrially viable options [19]. Accordingly, a multitubular fixed-bed reactor with Joule-heated walls is selected as the reference configuration. Both one- and two-dimensional reactor models are employed to ensure reliable prediction of temperature fields and cold-spot formation, which are critical aspects in the design of electrically heated packed-bed reactors [23–25]. On this basis, operability and performance diagrams are constructed to identify admissible operating envelope and optimized operating conditions and to provide structural insight into reactor behavior under variable design and operating parameters.

The proposed framework is demonstrated through a case study relevant to carbon capture and utilization, namely the reverse water–gas shift (rWGS) reaction, enabling the conversion of captured CO_2 into syngas using renewable hydrogen and supporting the production of e-derived fuels.

The article is organized as follows. Section 2 outlines the rWGS process and selected catalyst system. Section 3 describes the reactor models, while Section 4 introduces the stability-assessment methodology. Section 5 presents the results of the operability and performance analyses and discusses their implications for reactor design, control, and process intensification.

2. Process and constraints

The reverse water–gas shift reaction (rWGS, Eq. (1)) is a relevant endothermic route for CO_2 utilization and syngas upgrading [26] (Fig. 1). It enables the production of syngas with adjustable CO/H_2 ratios [27] and represents an upstream step for processes such as methanol synthesis [28] and Fischer–Tropsch pathways [29].

$$CO_2 + H_2 \rightleftharpoons CO + H_2O \;\; \Delta\widetilde{H}_{r,298K} = +41 \; kJ/mol \tag{1}$$

Electrified reactors offer an alternative to conventional furnace-heated systems by supplying the endothermic heat demand through electrical energy, potentially from renewable sources. In Joule-heated configurations, heat is generated directly within the reactor structure or catalyst bed, enabling compact layouts and improved controllability. However, the strong coupling between heat generation, temperature distribution, and reaction kinetics introduces additional constraints related to thermal management, spatial temperature gradients, and sensitivity to operating conditions. These aspects are particularly critical for rWGS, where insufficient heat supply or unfavourable temperature profiles may lead to cold-spot formation, reduced conversion, or enhanced methanation.

The feasible operating window of rWGS reactors is further constrained by thermodynamic limitations. Equilibrium conversion and CO selectivity strongly depend on temperature and feed composition, while low temperatures or H_2-rich conditions promote methanation and carbon formation [30]. These constraints become more severe under intensified operation, where high heat fluxes and compact geometries are combined. Accordingly, thermodynamic analysis represents a necessary first step to identify operating regions compatible with high CO_2 conversion, limited CH_4 formation, and catalyst stability [31,32]. This aspect is especially relevant for electrified reactors, where unconventional temperature profiles may push the system toward

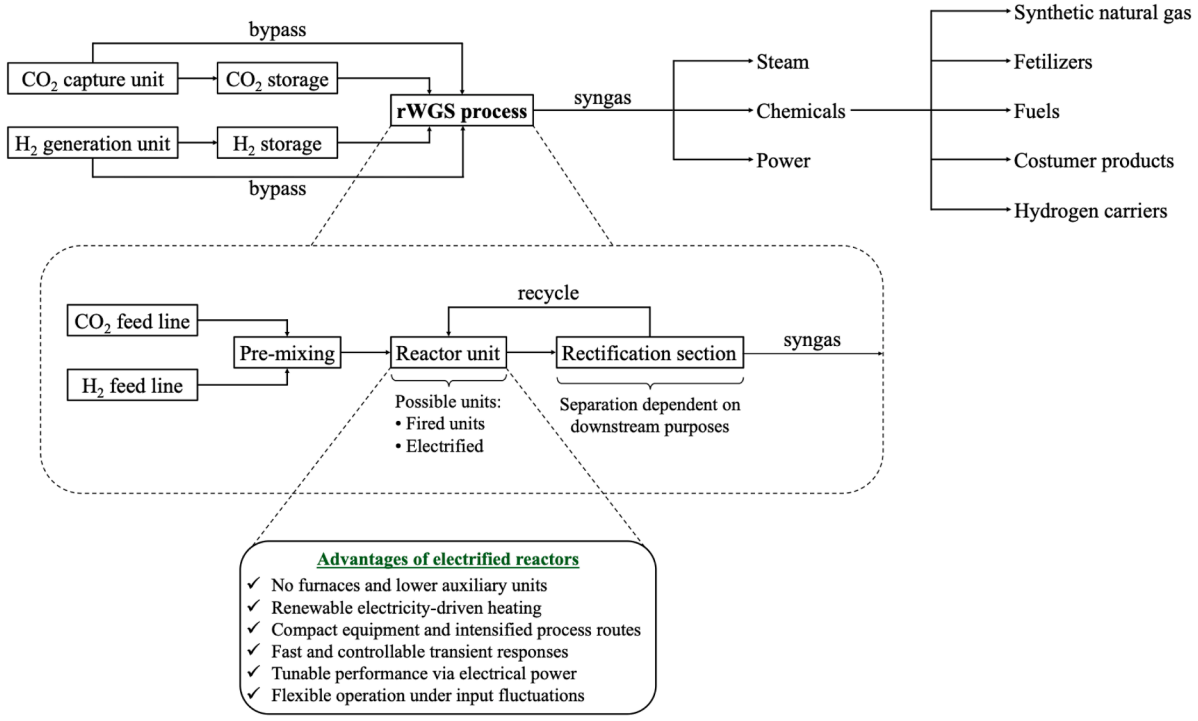

Fig. 1. rWGS within the CO_2 and hydrogen utilization value chain and role of electrified reactors.

thermodynamic boundaries.

Catalyst selection and kinetic description constitute an additional set of constraints for intensified and electrified rWGS operation. From a techno-economic standpoint, Ni-based catalysts provide a favourable compromise between activity, selectivity, and cost, while offering a sufficiently rich experimental and kinetic literature for predictive modelling. In contrast, Cu- and Fe-based systems are often limited by the availability of reliable kinetic models under high-temperature conditions [33,34], whereas noble metals remain constrained by cost [35–37]. Catalyst supports further influence thermal and mechanical stability [38], resistance to sintering, and tolerance to temperature gradients. Oxide supports such as Al_2O_3, SiO_2, ZnO, and CeO_2 are commonly employed to enhance thermal stability and mitigate deactivation [39–41]. Among common oxide supports, Al_2O_3 offers a suitable balance of high surface area, mechanical robustness, and moderate metal–support interactions, making Ni/Al_2O_3 catalysts particularly attractive for Joule-heated tubular reactors [42].

Based on these considerations, Ni/Al_2O_3 catalysts are adopted in the present work. Several literature kinetic models for rWGS over Ni-based catalysts are available [43–46]. However, their applicability to electrified reactors remains uncertain, as intensified heat input and steep temperature gradients may violate assumptions underlying furnace-based regressions. A systematic comparison of selected kinetic models is therefore performed to identify a suitable formulation for predictive modelling and stability analysis under electrified operating conditions.

3. Reactor modelling

From a reactor-engineering perspective, the strongly endothermic nature of the rWGS reaction implies that process performance is often limited by heat transfer rather than intrinsic kinetics. Reactor intensification strategies must therefore primarily address heat-supply efficiency and temperature control, especially under high-throughput operation [47,48].

Among the available options, reactor electrification enables direct and controllable heat supply while preserving conventional catalyst formulations. Joule-heated wall reactors, which have recently reached commercial deployment in large-scale applications such as steam cracking [49,50], demonstrate the feasibility of decoupling heat generation from combustion while retaining established reactor concepts. In this work, a multitubular fixed-bed reactor with Joule-heated walls is selected as the reference configuration, owing to its industrial maturity, compact layout, favourable thermal efficiency, and moderate pressure-drop penalties for endothermic duties [51–53].

This configuration inherently involves a trade-off between heat-transfer efficiency and hydrodynamic performance. The ratio between the heat generated by reaction and the heat supplied through the tube wall scales with $4/D_{tubes}$, decreasing with increasing tube diameter. While larger diameters reduce pressure drop, they also impair radial heat transfer and may promote temperature gradients or cold-spot formation within the catalytic bed [54]. Accurate prediction of temperature fields is therefore essential for reactor design and stability assessment.

To address this aspect, two reactor models with different spatial resolution are implemented and cross-compared: a one-dimensional (1D) axial model and a two-dimensional (2D) axisymmetric model. This hierarchical approach combines rapid design-oriented analysis with higher-fidelity assessment of radial transport limitations, providing a consistent basis for evaluating thermal behaviour, cold-spot formation, and operability of electrified endothermic reactors. The present model assumes approximately uniform volumetric Joule heating within the reactor wall. Potential electrothermal effects associated with strongly temperature-dependent electrical resistivity or localized contact resistances are not explicitly considered and may affect the detailed temperature distribution under certain operating conditions.

3.1. 1D model

The one-dimensional (1D) model resolves the reactor along the axial coordinate z only [55], neglecting radial and circumferential gradients. Despite this simplification, it retains interphase transport and intraparticle mass- and heat-transfer effects, making it suitable for preliminary design, optimization, and sensitivity analyses.

The model consists of fluid-phase mass and energy balances formulated as ordinary differential equations (ODEs), coupled with algebraic equations (AEs) describing wall and catalyst behaviour. At each axial location, local intraparticle problems are solved to evaluate the effectiveness factors entering the bulk-fluid balances.

Joule heating is modeled by imposing the electrical current flowing through each reactor tube and calculating the corresponding volumetric heat-generation term from the tube electrical resistivity and wall geometry. The electrical resistivity of the tube material is reported in the Supplementary Material, while the corresponding tube resistance can be determined from the tube dimensions and material properties. The model therefore assumes imposed-current operation at the tube level; detailed electrical-engineering aspects of the reactor assembly (e.g., electrical connection schemes or power-electronics architecture) are beyond the scope of the present reactor-scale analysis.

The full set of governing equations and boundary conditions is reported in Tables 1 and 2, respectively, while the relevant dimensionless groups are listed in the Nomenclature. A schematic representation of the modelling framework is provided in Fig. 2.

The reactor domain is divided into three regions: wall, fluid, and catalyst particles. Since no mass transfer or chemical reaction occurs within the wall, only an energy balance is considered [56]. Joule heating is assumed spatially uniform [57] and is coupled to the fluid through an overall heat-transfer coefficient [58]. The present model assumes approximately uniform volumetric Joule heating within the electrically resistive reactor wall. This approximation is considered reasonable for the investigated FeCrAl-based tube material, whose electrical resistivity exhibits comparatively limited variation over the operating-temperature range considered here, as discussed in the Supplementary Material. More generally, stronger temperature-dependent resistivity variations or localized electrical-contact effects could generate non-uniform heating distributions, potentially affecting the detailed thermal field and influencing the intensity or position of cold-spot and high-temperature regions.

Axial and radial conduction within the wall are neglected. This assumption is considered reasonable for the present steady-state Joule-heated configuration because thermal energy is generated continuously along the electrically resistive tube wall rather than being supplied from localized external heating sources. Consequently, no pronounced axial temperature discontinuities are expected within the wall, and axial conductive redistribution is expected to play a secondary role compared with radial heat transfer and axial conductive transport. Under these conditions, radial heat transfer from the wall toward the reacting fluid constitutes the dominant thermal mechanism, whereas axial heat redistribution through wall conduction is expected to play a secondary role relative to axial convective transport in the reacting flow. This interpretation is consistent with preliminary sensitivity checks performed during model development. Moreover, the relatively small Biot number (Eq. 2) indicates limited internal thermal resistance across the wall thickness, supporting the assumption of an approximately uniform wall temperature in the radial direction.

Table 1
Governing mass and energy balance equations for the 1D axial reactor model.

Mass balance (Reactive fluid)	$\frac{\partial u_i}{\partial z} = -\xi_{m,i}\left(u_i - u_{i,s,cat}\right)$
Mass balance (External catalyst's surface)	$0 = \xi_{m,i}\left(u_{i,s,cat} - u_i\right) + \nu_{i,f}\eta_f Da R_f + \nu_{i,b}\eta_b Da R^{in}_{r(b,f)} R_b$
Mass balance (Internal catalyst's domain)	$0 = \frac{\Xi^2_{tubes}}{\Xi^2_{cat}}\frac{1}{Pe_{m,cat}}\left(\frac{\partial^2 u_{i,cat}}{\partial r^2_{cat}} + \frac{2}{r_{cat}}\frac{\partial u_{i,cat}}{\partial r_{cat}}\right) + \nu_{i,f} Da R_f + \nu_{i,b} Da R^{in}_{r(b,f)} R_b$
Energy balance (Reactive fluid)	$\frac{\partial \Theta}{\partial z} = St(\Theta_{wall} - \Theta) - \xi_T(\Theta - \Theta_{s,cat})$
Energy balance (Electrified wall)	$\varphi_{wall} St(\Theta_{wall} - \Theta) = \beta\gamma\Xi^2_{tubes}\mho$
Energy balance (External catalyst's surface)	$0 = \xi_T(\Theta - \Theta_{s,cat}) + \eta_f B Da R_f + \eta_b B Da R_b H_{r(b,f)} R^{in}_{r(b,f)}$
Energy balance (Internal catalyst's domain)	$0 = \frac{\Xi^2_{tubes}}{\Xi^2_{cat}}\frac{\varphi_{cat}}{Pe_T}\left(\frac{\partial^2 \Theta_{cat}}{\partial r^2_{cat}} + \frac{2}{r_{cat}}\frac{\partial \Theta_{cat}}{\partial r_{cat}}\right) + B\varphi_{cat} Da R_f + B\varphi_{cat} Da R_b H_{r(b,f)} R^{in}_{r(b,f)}$
Momentum balance (Reactive fluid)	$\frac{\partial \mathscr{P}}{\partial z} = -a r_z - b r_z^2$

Table 2
Boundary conditions for the 1D axial reactor model.

$z = 0 \rightarrow u_i = \frac{C_{i,inlet}}{C_{CO_2,inlet}}$	Inlet values
$z = 0 \rightarrow \Theta = 0$	
$z = 0 \rightarrow \mathscr{P} = 1$	
$r_{cat} = 0 \rightarrow \frac{\partial u_{i,cat}}{\partial r_{cat}} = 0$	Radial symmetry
$r_{cat} = 0 \rightarrow \frac{\partial \Theta_{cat}}{\partial r_{cat}} = 0$	
$r_{cat} = 1 \rightarrow u_{i,cat} = u_{i,s,cat}$	Local continuity
$r_{cat} = 1 \rightarrow \Theta_{cat} = \Theta_{s,cat}$	

$$Bi = \frac{h_T}{k_{T,wall}/t_{tubes}} \tag{2}$$

The catalyst surface is treated as an interfacial pseudo-domain where mass and energy balances account for convective exchange with the bulk fluid and heterogeneous reactions. Catalyst pellets are approximated as spheres [59]. Intraparticle transport limitations are accounted for through the effectiveness factor η, defined as the ratio between the volume-averaged reaction rate within the pellet and the rate evaluated at surface conditions (Eq. 3).

$$\eta = \frac{1}{V_{cat}}\frac{\int r_{cat}\, dV_{cat}}{r_s} \tag{3}$$

Because analytical correlations for η are typically limited to isothermal pellets and irreversible kinetics, they are not generally applicable to rWGS [60]. In the present work, the effectiveness factor is therefore not prescribed through analytical expressions but evaluated numerically at each axial position by solving the steady-state intraparticle mass and energy balances reported in Tables 1 and 2 as local auxiliary problems within the catalyst particle. The resulting effectiveness factors are subsequently introduced into the bulk-fluid and catalyst-surface balances as closure terms correcting the effective reaction rates. The intraparticle balances are therefore solved locally as auxiliary subproblems and are not reported as additional governing equations of the final reactor-scale formulation. Accordingly, the reactor equations reported in the 1D formulation correspond to the final coupled system after incorporation of the numerically evaluated effectiveness factors.

Overall, the 1D model provides a favourable compromise between physical fidelity and computational efficiency by explicitly accounting for interphase transport and intraparticle limitations while neglecting radial temperature gradients. However, the assumptions of spatially uniform Joule heating and negligible wall conduction limit its ability to capture radial temperature gradients and local thermal spots that may arise under electrified operation, motivating the adoption of a higher-dimensional model. The present reactor formulation is strictly steady state; accordingly, no temporal accumulation terms are included in the governing balances. The heat-capacity terms appearing in the dimensionless equations arise exclusively from the adopted non-dimensionalization procedure.

3.2. 2D model

The two-dimensional (2D) model resolves the reactor in cylindrical coordinates along the axial (z) and radial (r) directions, assuming axisymmetry and neglecting circumferential variations [61]. This

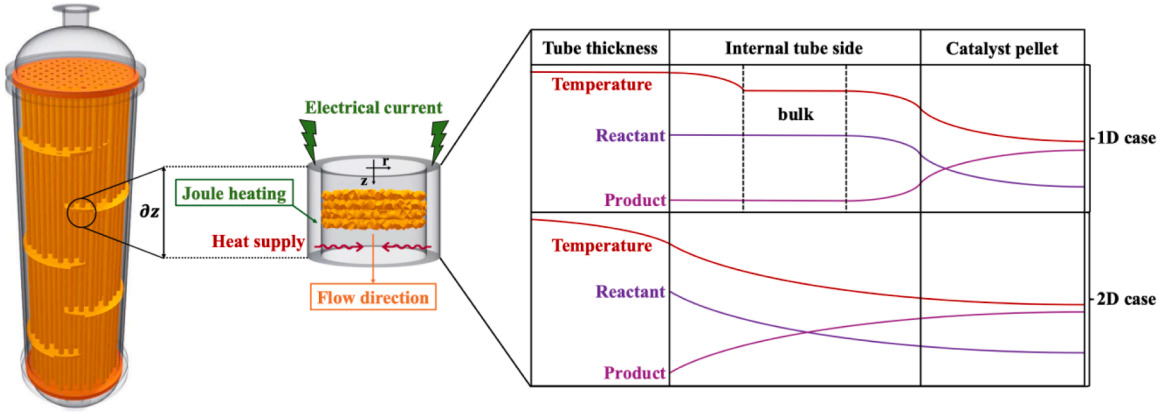

Fig. 2. Schematic of the Joule-heated multitubular reactor and comparison between 1D axial and 2D axisymmetric modeling approaches, highlighting wall–fluid–catalyst domains and temperature and concentration profiles.

formulation explicitly captures radial temperature and concentration gradients, which become increasingly relevant under intensified heat-transfer conditions and for larger tube diameters. In contrast to the 1D model, the 2D approach directly resolves coupled heat and mass balances within the catalyst phase, without relying on effectiveness-factor closures.

The governing mass and energy balance equations for the fluid, wall, and catalyst domains are reported in Table 3, while the associated boundary conditions are summarized in Table 4. Additional dimensionless groups specific to the 2D formulation are listed in the Nomenclature.

The steady-state 2D formulation yields a coupled set of partial differential equations (PDEs), which are solved using the method of lines (MOL). Radial derivatives are discretized via finite differences, resulting in a system of ordinary differential equations integrated along the axial coordinate using a stiff solver. Joule heating is assumed spatially uniform within the tube wall [62,63], and heat transfer to the fluid occurs radially [64].

Thermal equilibrium and flux continuity are imposed at the wall–fluid interface, while the external wall boundary is treated as adiabatic, consistent with a multitubular configuration with limited external heat losses. Axial wall conduction is neglected consistently with the 1D formulation. In the present steady-state Joule-heated configuration, thermal energy is generated volumetrically along the electrically resistive wall, such that radial heat transfer toward the reacting fluid remains the dominant thermal mechanism. Additional simulations including axial wall conduction showed negligible effects on the predicted reactor behaviour within the investigated operating window.

The catalyst bed is assumed radially homogeneous, while intraparticle transport and reaction are resolved along the radial coordinate through effective thermal conductivity and diffusivity. Local fluid temperature and concentration fields provide boundary conditions for solid-phase transport and reaction, ensuring consistent coupling between fluid and catalyst phases. This formulation enables direct identification of radial transport limitations and temperature non-uniformities, including cold-spot formation, which may constrain intensified operation.

Overall, the 2D axisymmetric model substantially increases physical fidelity by explicitly resolving radial gradients and fluid–solid coupling without effectiveness-factor closures. This allows mechanistic assessment of wall-driven hot and cold spots and non-uniform catalyst utilization. However, the increased computational cost and remaining assumptions—such as uniform Joule heating, radial bed homogeneity, and negligible axial wall conduction—may render the 2D model unnecessary in operating regimes where the 1D formulation already provides an adequate description of reactor behaviour.

Table 3
Governing mass and energy balance equations for the 2D axisymmetric reactor model.

Mass balance (Reactive fluid)	$\frac{\partial u_i}{\partial z} = \frac{\Xi^2_{tubes}}{Pe_{m,r}} \frac{1}{r} \frac{\partial}{\partial r}\left(r \frac{\partial u_i}{\partial r}\right) - \frac{\Xi^2}{\Xi^2_{cat}} \frac{2}{Pe_{m,cat}} \frac{\partial u_{i,cat}}{\partial r_{cat}}\Big\|_{r_{cat}=R_{cat}}$
Mass balance (Internal catalyst's domain)	$0 = \frac{\Xi^2_{tubes}}{\Xi^2_{cat}} \frac{1}{Pe_{m,cat}} \left(\frac{\partial^2 u_{i,cat}}{\partial r^2_{cat}} + \frac{2}{r_{cat}} \frac{\partial u_{i,cat}}{\partial r_{cat}}\right) + \nu_{i,f} Da R_f + \nu_{i,b} Da R^{in}_{r(b,f)} R_b$
Energy balance (Reactive fluid)	$\frac{\partial \Theta}{\partial z} = \frac{\Xi^2}{Pe_T} \frac{1}{r} \frac{\partial}{\partial r}\left[r \frac{\partial \Theta}{\partial r}\right] - \frac{\Xi^2}{\Xi^2_{cat}} \frac{2}{Pe_T} \frac{\partial \Theta_{cat}}{\partial r_{cat}}\Big\|_{r_{cat}=R_{cat}}$
Energy balance (Electrified wall)	$0 = \frac{\varphi_{wall}}{Pe_T} \frac{\zeta}{r} \frac{1}{r} \frac{\partial}{\partial r}\left(r \frac{\partial \Theta_{wall}}{\partial r}\right) + \beta^2 \gamma \mathfrak{V}$
Energy balance (Internal catalyst's domain)	$0 = \frac{\Xi^2_{tubes}}{\Xi^2_{cat}} \frac{\varphi_{cat}}{Pe_T} \left(\frac{\partial^2 \Theta_{cat}}{\partial r^2_{cat}} + \frac{2}{r_{cat}} \frac{\partial \Theta_{cat}}{\partial r_{cat}}\right) + B \varphi_{cat} Da R_f + B \varphi_{cat} Da R_b H_{r(b,f)} R^{in}_{r(b,f)}$
Momentum balance (Reactive fluid)	$\frac{\partial \mathscr{P}}{\partial z} = -a r_z - b r_z^2$

Table 4
Boundary conditions for the 2D axisymmetric reactor model.

$z = 0 \rightarrow u_i = \frac{C_{i,inlet}}{C_{CO_2,inlet}}$	Inlet value
$z = 0 \rightarrow \Theta = 0$	
$z = 0 \rightarrow \mathscr{P} = 1$	
$r = 0 \rightarrow \frac{\partial u_i}{\partial r} = 0$	Radial symmetry
$r = 0 \rightarrow \frac{\partial \Theta}{\partial r} = 0$	
$r = 1 \rightarrow \frac{\partial \Theta}{\partial r} = \zeta \frac{\partial \Theta_{wall}}{\partial r}$	Local flux continuity
$r = 1 \rightarrow \frac{\partial u_i}{\partial r} = 0$	Absence of mass flux(es)
$r = 1 \rightarrow \Theta_{wall} = \Theta$	Local continuity
$r = 1 + \frac{s_{tubes}/2}{D_{tubes}/2} \rightarrow \frac{\partial \Theta_{wall}}{\partial r} = 0$	Insulated tube
$r_{cat} = 0 \rightarrow \frac{\partial u_{i,cat}}{\partial r_{cat}} = 0$	Radial symmetry
$r_{cat} = 0 \rightarrow \frac{\partial \Theta_{cat}}{\partial r_{cat}} = 0$	
$r_{cat} = 1 \rightarrow u_{i,cat} = u_{i,s,cat}$	Local continuity
$r_{cat} = 1 \rightarrow \Theta_{cat} = \Theta_{s,cat}$	

4. Stability assessment

To support reactor design and operation under intensified conditions, an operability assessment is performed. Mapping reactor response over broad operating ranges enables identification of regimes in which small variations in inputs or parameters induce disproportionate changes in temperature and performance, thereby constraining feasible design, operation, and control. This aspect is particularly relevant for

electrified reactors, where high and spatially non-uniform heat fluxes, steep temperature gradients, and dynamic power modulation may amplify parametric sensitivities and affect operability and controllability.

For reacting systems, the parametric sensitivity framework developed by Varma, Morbidelli, and Wu (VMWT) is widely adopted [65]. Although originally introduced for the analysis of thermal runaway in exothermic reactors, the framework can be extended to endothermic systems by solving the governing mass and energy balances together with the associated sensitivity equations. These equations are obtained by differentiating the balance equations with respect to a selected model parameter and linking the result to an observable of interest. In this work, the selected observable is the normalized sensitivity of the dimensionless temperature Θ with respect to the dimensionless heat of reaction B, denoted $S(\Theta;B)$ [66] and defined in Eq. 4.

$$S(\Theta;B)=\frac{B}{\Theta}\frac{\partial\Theta}{\partial B}=\frac{B}{\Theta}s(\Theta;B) \tag{4}$$

Implementation of the VMWT framework therefore requires differentiating the governing balance equations with respect to B [67]. For the present multidimensional non-isothermal reactor formulation, the full sensitivity equations are not reported explicitly because of the complexity of the coupled governing equations. The corresponding equations were implemented numerically within the reactor solver. Differentiation was applied only to the explicit occurrences of the selected sensitivity variable (dimensionless temperature), whereas implicitly temperature-dependent properties were not further differentiated.

Because the adopted dimensionless temperature definition imposes $\Theta = 0$ at the reactor inlet, the normalized sensitivity coefficient formally becomes singular at $z = 0$. This localized singularity is solely a consequence of the normalization procedure and is confined to the inlet boundary point. The sensitivity analysis is therefore performed over the reactor domain excluding the inlet point, where Θ remains finite.

The resulting analysis yields operability and performance maps that are used to delimit feasible operating regions, identify regime transitions, and interpret reactor behaviour under intensified or variable operating conditions. For electrified reactors, these maps provide a compact representation of operating domains in which perturbations in electrical power input, wall temperature, or feed conditions may trigger large thermal or kinetic responses.

Steady-state operating-regime diagrams are reported as *Da*–*B* parametric maps, where *Da* denotes a generalized Damköhler-type dimensionless reactivity index representing the ratio between characteristic reaction and transport times, while B denotes a dimensionless thermal-effect parameter expressing the relative magnitude of reaction-enthalpy effects with respect to the sensible thermal capacity of the reacting system. The adopted notation follows the generalized VMWT formulation, where *Da* and B are respectively used as the principal reactivity and thermal coordinates of the operating-regime maps. Moreover, the term 'parametric map' is adopted here to avoid ambiguity with other uses of the term 'phase diagram' [68,69]. Here, the use of B as the principal thermal coordinate follows the classical VMWT framework for sensitivity-based operability analysis. Within this formulation, regime-transition boundaries are identified as intrinsic features of the reactor steady-state thermal behaviour [5]. Consequently, different perturbation variables generally identify similar regime-transition boundaries, although with different operational interpretations. The choice of B is motivated by its ability to compactly incorporate the combined thermal effects of multiple inlet and process variables into a single generalized thermal coordinate.

The Da–B maps therefore provide a generalized representation of the reactor thermal-operability structure, whereas the subsequent analyses based on current, flow rate, and inlet temperature provide the corresponding operational interpretation in terms of practically controllable variables.

The regime-transition boundaries reported in the *Da*–*B* diagrams are obtained by systematically solving the reactor model over the investigated *Da*–*B* domain and identifying changes in the qualitative structure of the axial temperature profile together with the corresponding thermal-operability limits [5,70]. In particular, cold-spot operation (CSO) is identified by the presence of an internal axial temperature minimum along the reactor length. Operating conditions without an internal temperature minimum are classified either as pseudo-adiabatic operation (PAO) or high-temperature operation (HTO), depending on the corresponding thermal behaviour. PAO corresponds to thermally admissible operating conditions characterized by relatively moderate temperature variations, whereas HTO corresponds to overheating conditions characterized by monotonically increasing temperature profiles and progressively increasing reactor temperatures. Under these conditions, outlet temperatures may exceed the admissible operating window associated with catalyst and reactor-material limitations. In contrast to classical hot spots in exothermic reactors, the HTO regime identified here does not necessarily involve the formation of an internal temperature maximum, since the highest temperatures are generally reached near the reactor outlet. Within the present operating domain, only the first cold-spot regime (CSO_1) is observed. A second cold-spot regime (CSO_2), typically associated with the occurrence of an internal maximum in the target-product yield, is not identified under the investigated conditions.

The corresponding performance diagrams are obtained by evaluating conversion, yield, selectivity, and outlet temperature along the identified regime-transition boundaries.

Although thermal runaway is not expected in endothermic systems, regions of high parametric sensitivity can still be identified by large values of $S(\Theta;B)$. These sensitivity-dominated domains (SENS), analogous to runaway regions in exothermic reactors, indicate operating conditions in which small parameter variations induce large changes in reactor response [71]. In electrified reactors, such regions are of particular concern, as fluctuations in electrical power input or heat-transfer conditions may directly translate into significant temperature excursions, limiting robustness and controllability.

Within the present VMWT-based framework, these maps characterize the steady-state sensitivity and operability of the reactor with respect to variations in thermal and operating conditions. The analysis therefore focuses on identification of regime transitions, thermal robustness, and thermally sensitive operating regions, rather than on transient dynamic stability obtained through eigenvalue analysis.

Reactor performance is evaluated through bifurcation plots of conversion, yield, and selectivity across regime transitions, where a state variable is plotted as a function of a system parameter [72,73]. The combined use of operating-regime maps and performance indicators enables systematic identification of thermally admissible high-performance operating regions while supporting robust and controllable reactor operation under intensified and electrified conditions. For the endothermic rWGS system considered here, the formal definition of B yields negative values owing to the positive reaction enthalpy. However, the operating-regime maps are represented using |B| solely as a plotting convention for consistency with the canonical VMWT graphical representation. The underlying sensitivity formulation remains fully based on the original signed definition of B.

5. Results and discussion

Section 5 presents the main results of the study. Section 5.1 defines the reference operating conditions and kinetic model derived from the thermodynamic and kinetic analysis. Section 5.2 discusses the reference reactor design and the complementary use of the 1D and 2D models. Section 5.3 introduces the stability and performance diagrams, highlighting operating regimes and design and control limitations, while Section 5.4 illustrates their use for control and process intensification through inlet-condition variations.

5.1. Reference system and modeling assumptions

The reference system investigated in this work is a Joule-heated multitubular fixed-bed reactor arranged on a triangular pitch, as commonly adopted in shell-and-tube designs. This configuration provides high compactness and eliminates the need for external heating media and associated piping by relying on direct electrical heating [74], making it well suited for compact, modular, and electrically heated reactor concepts. The fixed bed consists of randomly packed catalyst pellets, and a commercial Ni/Al_2O_3 catalyst is selected for rWGS operation, as discussed in Section 2 [32]. FeCrAl is chosen as tube material due to its stable electrical resistivity over a wide temperature range, which is essential for predictable and controllable Joule heating under variable-power operation [75]. Additional physicochemical properties are provided in the Supplementary Material and are based on the data reported in [76–80].

Thermodynamic and kinetic screenings are performed to define suitable operating conditions and a reference kinetic model for electrified rWGS operation. Equilibrium calculations are carried out to identify operating windows compatible with high CO_2 conversion and CO selectivity, limited CH_4 formation, and avoidance of carbon deposition. The analysis confirms the strong influence of temperature, pressure, and feed composition on reactor performance, in agreement with established rWGS behaviour. High temperatures suppress methanation and solid carbon formation, while moderate pressures provide a compromise between conversion, selectivity, and compression requirements—an especially relevant trade-off for electrically heated reactors. Although the ideal-gas rWGS equilibrium is formally pressure independent because no net variation in the total number of moles occurs, pressure still affects the overall reacting system through secondary reactions, particularly methanation, together with coupled kinetic and transport effects. Full details of the thermodynamic screening are provided in the Supplementary Material, with the underlying methodology described in [81].

Several literature kinetic models for rWGS over Ni-based catalysts [43–46] were comparatively evaluated under identical electrified-reactor conditions to assess their consistency in predicting thermal behaviour, CO_2 conversion, and CH_4 formation. The corresponding axial temperature and species profiles are reported in the Supplementary Material (Fig. S2). The objective of this comparison was not to perform a full experimental validation of the kinetic expressions, but rather to select a literature model capable of consistently describing the coupled thermal and compositional behaviour of the reactor under the investigated operating conditions. Although the present work focuses on rWGS reactor behaviour, the adopted kinetic mechanisms also account for secondary reaction pathways responsible for methane formation. Accordingly, species such as CH_4 arise directly from the selected literature kinetic model rather than from independently introduced auxiliary reaction schemes. Among the models considered, the formulation by Vázquez et al. provided thermal and compositional trends most consistent with the behaviour of the investigated electrified rWGS reactor and was therefore selected as the reference kinetic model for the present operability analysis. The comparison should be interpreted as a qualitative consistency assessment rather than as a rigorous kinetic-validation study. The investigated operating conditions were selected to remain within, or reasonably close to, the applicability ranges reported in the original source papers, thereby avoiding substantial extrapolation of the adopted kinetic formulations. Carbon-formation tendencies discussed in the manuscript are inferred from thermodynamic considerations rather than from explicit carbon-deposition kinetics.

With respect to reactor modelling, multitubular fixed-bed reactors are analysed at the single-tube level, assuming nominally identical operation of all tubes in the bundle [82]. The inlet H_2/CO_2 ratio is selected to obtain an outlet syngas composition compatible with downstream methanol-synthesis processing, and each tube is fed at 0.1 kmol h^{-1}, corresponding to realistic industrial throughputs [83]. The investigated rWGS reactor should be interpreted as an upstream syngas-generation unit rather than as a direct methanol-synthesis feed generator. Accordingly, downstream conditioning steps, such as CO_2 separation/recycle and/or H_2 adjustment, may be required before achieving the desired methanol-synthesis feed specifications. Under these assumptions, the H_2/CO ratio remains a meaningful indicator of the conditioned CO-rich syngas stream.

The operating temperature is constrained to remain above the carbon-formation threshold and below 950°C to avoid catalyst sintering and tube plugging [32,84]. Tube length is limited to 6 m to avoid non-standard designs.

Electrical current is adopted as the primary heating input, enabling operation within standard industrial voltage levels (220 ÷ 240 V; 480 ÷ 600 V) [85–88]. In this configuration, current directly determines the Joule-heating rate and strongly influences wall temperature, while electrical power demand follows from the available site voltage. The present formulation assumes imposed-current operation at the individual tube level, whereas detailed electrical-engineering aspects of large-scale reactor assemblies are not explicitly represented, consistent with the simplified but physically explicit electrical-heating framework adopted in this work. For the selected wall thickness (2.5 mm), wall–fluid heat-transfer coefficient ($h_T = 150\ Wm^{-2}K^{-1}$) [85], and wall thermal conductivity ($k_{T,wall} = 16\ Wm^{-1}K^{-1}$) [89,90], the resulting Biot number ($Bi = 0.023$) indicates negligible internal conduction resistance relative to convection, supporting the assumption of nearly uniform wall temperature across the tube thickness. The constant h_T value is employed exclusively for preliminary Biot-number estimations and simplified thermal assessments, and represents the average heat-transfer coefficient under the reference operating conditions. The full reactor simulations and operating-regime maps are instead obtained by solving the coupled transport equations, where local heat-transfer behaviour is determined directly by the governing conservation equations and local thermophysical conditions.

5.2. Reactor design

The reference reactor configuration adopted for subsequent analyses is summarized in Table 5, including inlet conditions, operating parameters, and key geometrical specifications. Operating temperature and pressure are selected based on the thermodynamic/kinetic screening while accounting for the predicted pressure drop along the tube, and the feed flow rate is set according to standard fixed-bed design practice [83]. The inlet H_2/CO_2 ratio and electrical current are chosen to achieve an outlet syngas ratio consistent with methanol synthesis ($H_2/CO \approx 2$). Tube length and current intensity are then adjusted to meet the target outlet composition.

5.2.1. 1D reactor modelling

Fig. 3 reports the axial profiles of temperature, conversion, and dimensionless species predicted by the steady-state 1D reactor model under the reference operating conditions listed in Table 5. The results show the formation of an axial cold spot close to the reactor inlet

Table 5
Reference operating conditions and geometrical parameters defining the reactor configuration.

Quantity	Symbol	Value
Inlet temperature	T_{in}	750°C
Operating pressure	P	2.5 bar
Inlet molar flow rate (per tube)	$\dot{n}_{in,tube}$	0.1 kmol h^{-1}
H_2/CO_2 inlet molar ratio	$y^{in}_{H_2}/y^{in}_{CO_2}$	1.86
Tube length	L_{tubes}	6 m
Tube diameter	D_{tubes}	25 mm
Tube wall thickness	t_{tubes}	2.5 mm
Electrical current (per tube)	I_{tubes}	75 A

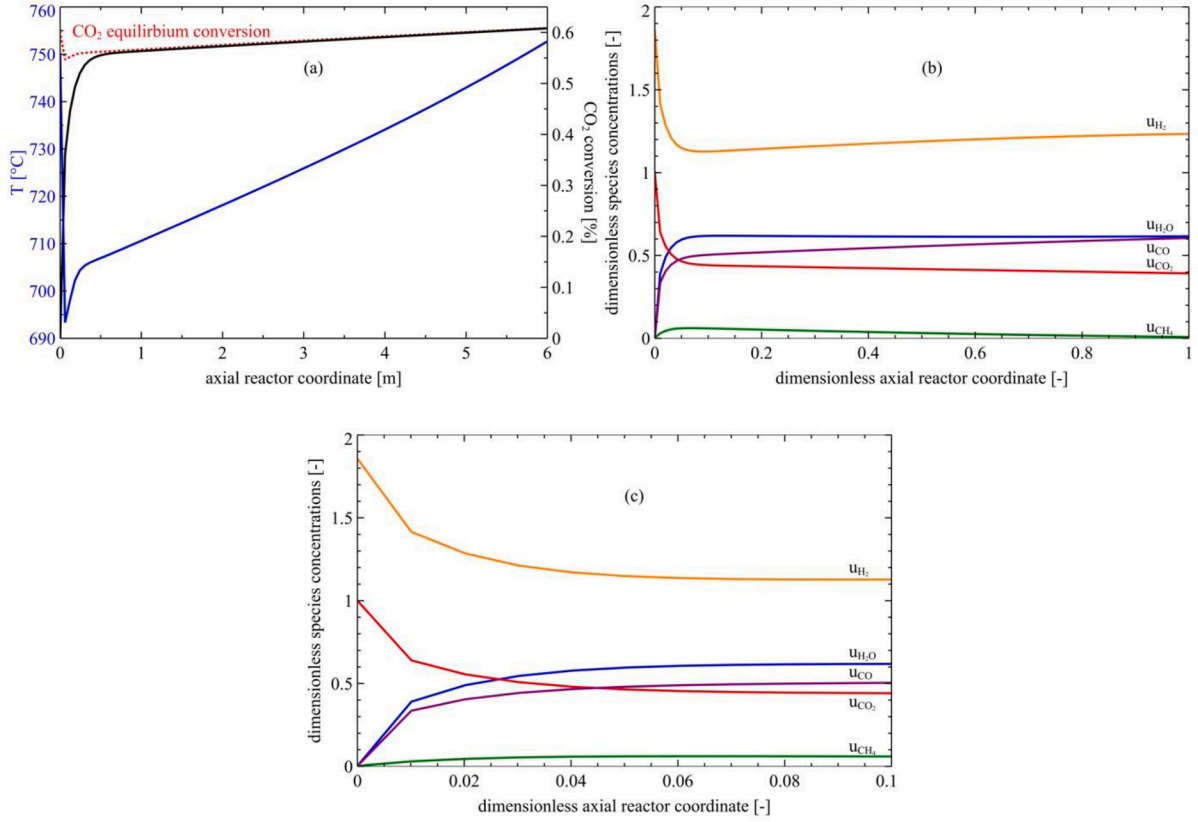

Fig. 3. Axial profiles predicted by the 1D steady-state reactor model: (a) temperature and CO_2 conversion, including the corresponding local thermodynamic-equilibrium conversion; (b) dimensionless species concentrations normalized by the inlet CO_2 concentration; (c) enlarged view of the inlet region (first 0.6 m). Operating conditions from Table 5 (inlet pressure 2.5 bar; inlet concentration 10.29 mol m^{-3}).

($z < 0.1\ m$), driven by the strong endothermicity of the rWGS reaction under high reactant concentrations. The associated heat uptake leads to a local temperature minimum, followed by temperature recovery downstream as Joule heating progressively exceeds the reaction heat demand and the approach to equilibrium reduces the net reaction rate [91].

For the selected inlet composition ($H_2/CO = 1.86$), the model predicts a CO_2 conversion of approximately 60% and an outlet H_2/CO ratio close to 2, consistent with syngas specifications for methanol synthesis. The predicted temperature profile remains within the range 650 ÷ 950°C, thereby avoiding conditions associated with carbon formation, catalyst deactivation, or sintering [84]. Pressure decreases along the tube due to frictional losses, reaching approximately 1.35 bar at the outlet.

Fig. 3 additionally reports the local thermodynamic-equilibrium CO_2 conversion profile evaluated at the axial temperature and pressure predicted by the reactor model. The comparison between nominal and equilibrium conversion shows that the reactor operates relatively close to the local thermodynamic limit over most of the reactor length. The largest deviations occur in the inlet cold-spot region, where the sharp temperature decrease locally reduces reaction rates and enhances kinetic and transport limitations. Downstream of the cold spot, progressive temperature recovery promotes closer approach to equilibrium conditions.

CH_4 formation is concentrated in the cold-spot region and becomes negligible downstream, consistent with thermodynamic expectations at elevated temperatures. The low-temperature environment generated by the inlet cold spot favours hydrogenation activity and methane formation under H_2-rich conditions. However, carbon-deposition propensity cannot be inferred directly from methane concentration alone, as it also depends on CO activity, steam concentration, local thermodynamic conditions, and catalyst surface chemistry.

The maximum CH_4 concentration does not necessarily coincide with the axial temperature minimum. In the reference case, the minimum temperature occurs at approximately 0.06 m, whereas the maximum CH_4 concentration is reached further downstream at approximately 0.42 m. This behaviour reflects finite-rate kinetic and residence-time effects, which introduce an axial delay between the establishment of favourable low-temperature conditions and the subsequent accumulation of methane. Nevertheless, the broader set of simulations reported in the Supplementary Material shows that the methane maximum remains closely associated with the coldest reactor region across the investigated operating conditions. Furthermore, additional calculations performed under isothermal conditions at the inlet temperature show that the methane maximum remains present, although its magnitude is reduced by more than a factor of two compared with the nominal non-isothermal case. This observation indicates that methane formation is influenced by both local kinetic effects, associated with the high reactant concentrations present in the inlet region and the resulting methanation activity, and by the axial thermal field generated by cold-spot formation. The lower temperatures reached within the cold-spot region substantially enhance methane formation, consistent with the thermodynamic trends reported in the Supplementary Material.

The sensitivity of the axial temperature profile to the applied electrical current is illustrated in Fig. 4. Increasing the current above the design value primarily enhances downstream temperature recovery and outlet temperature, while the position and depth of the inlet cold spot remain comparatively weakly affected. This behaviour reflects the fact that cold-spot formation is governed predominantly by the intense endothermic heat absorption occurring near the reactor inlet, where reactant concentrations and intrinsic reaction rates are highest.

Although the reactor is electrically heated, the investigated

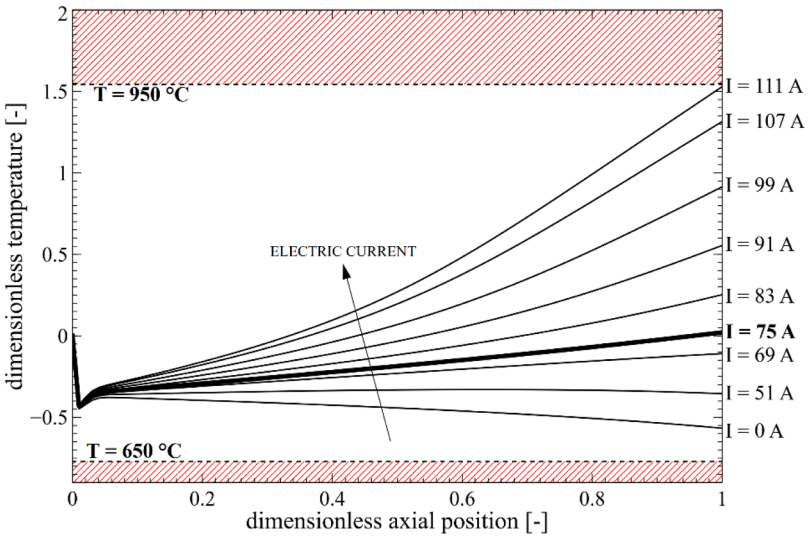

Fig. 4. Dimensionless axial temperature profiles for different electrical current levels (per tube), highlighting the admissible operating window.

configuration remains fundamentally a wall-heated tubular reactor in which thermal energy is generated volumetrically within the electrically resistive wall and subsequently transferred radially toward the reacting core. Consequently, classical tube-to-core heat-transfer limitations remain present despite the different heat-supply strategy relative to conventional furnace-heated systems. The cold spot forms very close to the reactor inlet, where reactant concentrations and intrinsic reaction rates are highest. Under these conditions, the intense local endothermic heat absorption initially exceeds the radial heat-transfer rate from the heated wall, leading to the formation of the inlet temperature minimum.

Conversely, the thermal effect of Joule heating develops progressively along the reactor length, such that variations in electrical current primarily influence downstream temperature recovery and outlet temperature while only partially affecting the inlet cold-spot structure. Notably, even under complete loss of electrical heating (I = 0 A), the minimum predicted temperature remains above the carbon-formation threshold under the investigated operating conditions, indicating favourable thermal behaviour of the selected reactor configuration.

Fig. 5 shows the effect of electrical current on outlet syngas composition. Increasing current raises the overall temperature level, enhancing conversion and shifting the outlet composition toward higher CO/H_2 ratios, whereas reduced current lowers conversion and yields CO/H_2 ratios below the target value. At the upper end of the investigated range, the temperature may approach or exceed the limit (≈ 950°C), potentially promoting undesired reactions and accelerating sintering, even though FeCrAl can tolerate higher temperatures [32,89,92]. In compositional terms, higher-current operation tends to overshoot the target $CO/H_2 \approx 0.5$ (requiring H_2 make-up for methanol synthesis), while lower-current operation moves CO/H_2 below the target (implying CO_2 addition or H_2 removal). Within these trade-offs, 75 A represents the best compromise for the present design, ensuring operation within the allowable temperature window while delivering a syngas composition compatible with methanol synthesis.

Fig. 6 compares axial temperature and species profiles for the limiting cases of no electrical heating and near-maximum heating. In both cases, an inlet cold spot is observed, confirming that cold-spot formation is an intrinsic feature of the reactor thermal behaviour. Although increasing current partially attenuates the cold spot, its position and depth remain comparatively weakly affected, reflecting the dominant influence of inlet conditions and local reaction rates in the inlet reactor region. Downstream, temperature increases more steeply at higher current as Joule heating progressively dominates over reaction heat effects. At zero current, the thermal field is governed solely by reaction enthalpies. At high current, the inlet cold spot persists but

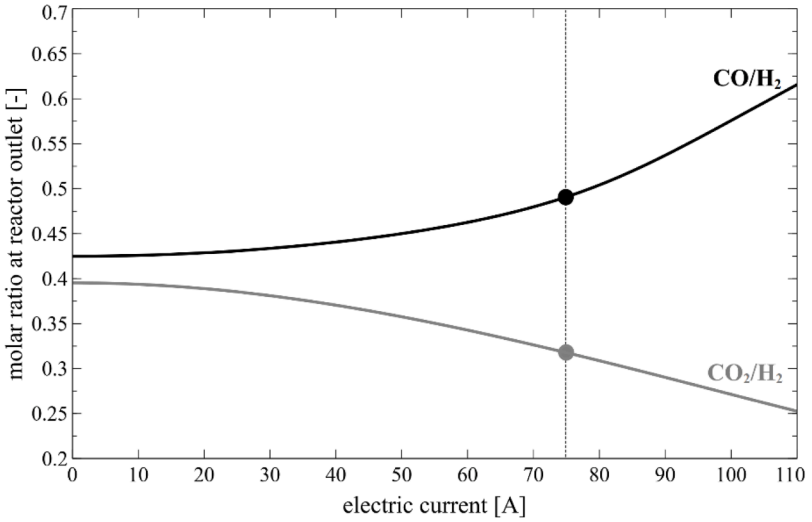

Fig. 5. Outlet molar ratios (CO/H_2 and CO_2/H_2) as a function of electrical current (per tube); markers indicate the reference design current (I = 75 A).

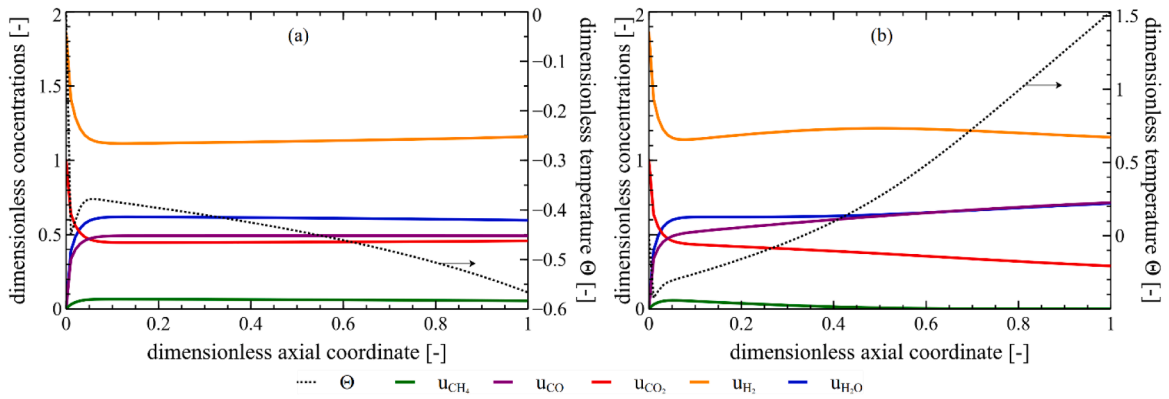

Fig. 6. Dimensionless axial temperature and species profiles predicted by the 1D model for the limiting electrical current levels: (a) 0 A (no heating) and (b) 111 A (upper operating limit in Fig. 4), per tube. Operating conditions from Table 5 (inlet temperature 750°C; inlet concentration 10.29 mol m^{-3}).

temperature recovers rapidly, promoting CH_4 consumption via reforming and sustaining rWGS progression, consistent with the monotonic CO_2 decrease.

5.2.2. 2D reactor modelling

The 2D model is employed to quantify radial transport effects and to assess the adequacy of the simplified 1D formulation under the investigated operating conditions. Table 6 compares the predictions of the two models under reference operating conditions, showing close agreement: outlet and minimum temperatures differ by approximately 1°C, and the predicted CO_2 conversion differs by less than 0.5%. The small discrepancies are attributed to the different treatment of the catalyst phase, represented through an effectiveness-factor closure in the 1D model and as a uniformly distributed solid phase in the 2D formulation. Both models predict operation within the targeted temperature window for high selectivity and catalyst stability.

Fig. 7 reports the steady-state 2D fields of temperature and CO_2 conversion. Conversion remains nearly uniform across the tube radius, whereas a limited radial temperature gradient is observed, with the minimum temperature located at the tube centre, farthest from the electrically heated wall. For the selected tube diameter (25 mm), the maximum radial temperature difference remains below 5°C, both in the inlet cold-spot region and near the reactor outlet. These results indicate that radial thermal gradients remain limited under the investigated operating conditions, supporting the applicability of the simplified 1D formulation.

In contrast, axial temperature variations are more pronounced, reflecting the strong endothermicity of the rWGS reaction and the higher reaction rates near the reactor inlet. Overall, the 2D results indicate that cold-spot formation is primarily an axial phenomenon under the investigated conditions, while radial non-uniformities exert only a limited influence on overall reactor behaviour. These findings support the use of the simplified 1D model for operability analysis and parametric studies within the investigated operating domain, whereas the 2D formulation provides a quantitative assessment of radial gradients and multidimensional transport effects.

Moreover, the close agreement between the models indicates that radial transport effects remain limited under the investigated operating conditions and for the selected compact tubular reactor geometry characterized by relatively small tube diameters. The purpose of the 2D analysis is not to demonstrate the breakdown of the 1D approximation, but rather to assess the relevance of multidimensional transport effects under operating conditions representative of electrified multitubular reactors. Larger tube diameters, lower effective radial thermal conductivity, or more extreme operating conditions could increase radial thermal gradients and potentially require more detailed multidimensional reactor descriptions. However, such conditions lie beyond the design domain considered in the present work, where relatively small tube diameters are adopted to favour efficient radial heat transfer and improved thermal management.

Table 6
Comparison between 1D and 2D model predictions for outlet temperature, minimum temperature, and CO_2 conversion under reference operating conditions (2D values are radius-averaged).

Quantity	Symbol	1D model	2D model
Outlet temperature	T_{out}	753°C	754°C
Minimum temperature	T_{min}	693°C	694°C
Outlet CO_2 conversion	$\chi_{CO_2}^{out}$	0.608	0.603

5.3. Operating-regime and performance diagrams

Operating-regime and performance diagrams are employed to interpret reactor behaviour and to support both design validation and operability assessment. Fig. 8 reports operating-regime maps constructed by varying the main geometrical design parameters of the system, thereby exploring how saturation of the available design degrees of freedom affects reactor behaviour. These maps provide a design-oriented perspective, highlighting the influence of reactor geometry and contact time on the attainable operating regimes and reactor performance.

In contrast, Fig. 9 focuses on operability and control by keeping the geometrical parameters fixed at the reference values reported in Table 5 and varying only the operating conditions. This second set of maps captures the reactor response to fluctuations in boundary inputs, such as electrical heating intensity and feed conditions, and is therefore directly relevant for control-oriented analysis. From a practical engineering perspective, these maps provide compact operating envelopes that can support reactor sizing, throughput selection, definition of thermally admissible electrical-current operating ranges, and control-oriented operation. In contrast to isolated parametric sweeps, the proposed representation directly identifies regime-transition boundaries together with the associated performance trends, enabling rapid assessment of how operating modifications or disturbances affect conversion, thermal behaviour, and operability margins.

This capability is particularly relevant for electrified reactors operating under variable renewable-power availability, where fluctuations in electrical input may shift the reactor operating point across different operating regimes. While the generalized Da–B maps provide the canonical representation adopted within the VMWT framework, the subsequent operability maps expressed in terms of electrical current, inlet temperature, and flow rate establish a direct connection with practically controllable reactor variables. Together, these complementary representations provide both a generalized description of reactor operating regimes and an engineering interpretation in terms of adjustable

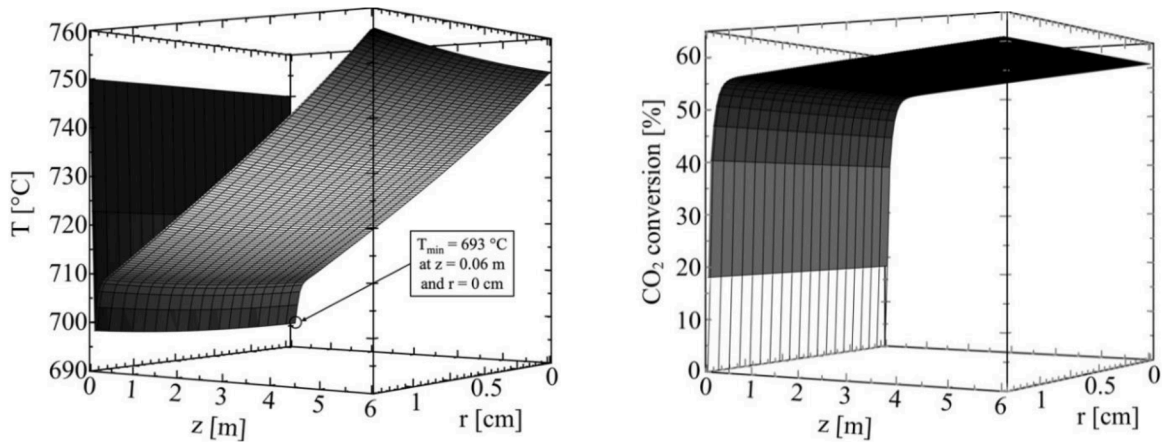

Fig. 7. Steady state 2D fields of temperature and CO_2 conversion, showing limited radial temperature gradients and a centreline cold spot near the reactor inlet.

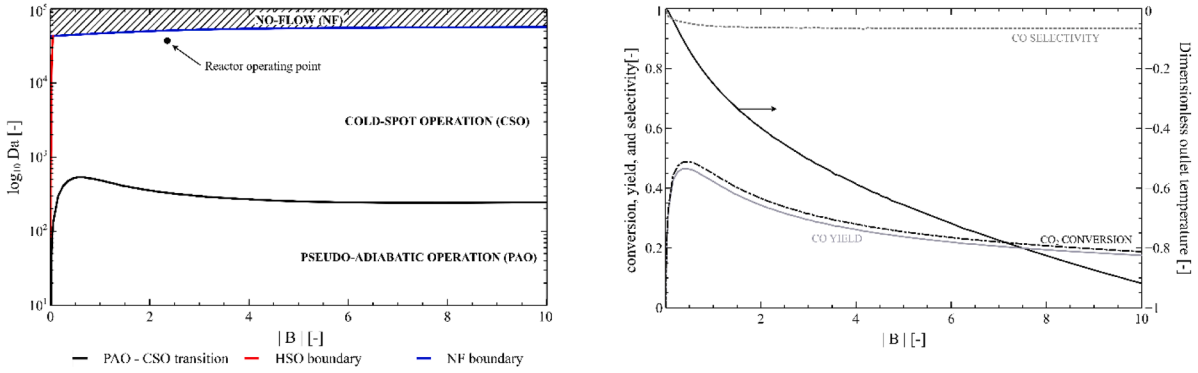

Fig. 8. Operating-regime map (left) and corresponding performance diagram (right) used for design validation. The reference operating point is highlighted. Operating regimes include pseudo-adiabatic operation (PAO), cold-spot operation (CSO), and no-flow (NF). Conversion, yield, selectivity, and dimensionless outlet temperature are evaluated along the PAO–CSO transition boundary. The shaded region indicates non-operable conditions. The CSO regime corresponds to operating conditions exhibiting an internal axial temperature minimum. The horizontal axis reports the absolute value |B| of the dimensionless thermal parameter for consistency with the canonical VMWT graphical representation.

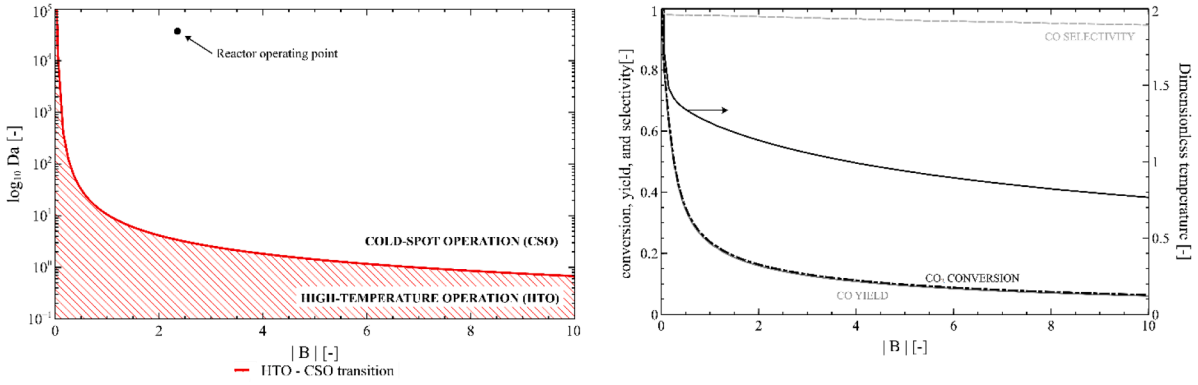

Fig. 9. Operating-regime map (left) and corresponding performance diagram (right) for operability analysis at the reference geometry (Table 5); the reference operating point is highlighted. Operating regimes include cold-spot operation (CSO) and high-temperature operation (HTO). Conversion, yield, selectivity, and dimensionless outlet temperature are evaluated along the HTO–CSO transition boundary. The shaded region corresponds to high-temperature operation characterized by monotonically increasing temperature profiles and progressive thermal accumulation along the reactor length. The horizontal axis reports the absolute value |B| of the dimensionless thermal parameter for consistency with the canonical VMWT graphical representation.

operating parameters.

For the reference reactor configuration investigated in this work, the nominal operating point remains well separated from the HTO boundary throughout the investigated operating range. This observation indicates that the selected reactor configuration operates with appreciable thermal-operability margins under the considered conditions. Accordingly, the proposed framework can be used not only to identify regime-transition boundaries, but also to quantify operability margins and assess the effects of operating-condition variations on reactor performance and thermal behaviour.

In both cases, performance diagrams are constructed by tracking the locus of points corresponding to the transition between pseudo-adiabatic operation (PAO) and cold-spot operation (CSO). This transition represents the dominant operating-regime boundary of the system and provides a compact descriptor of its overall behaviour. Along the investigated *Da*–*B* domain, operating points located above the PAO–CSO transition boundary are associated with higher reactor temperatures and improved reactor performance, as reflected by higher conversion and product yield. Conversely, operating points below the boundary correspond to lower-temperature operating conditions and reduced performance levels. Importantly, these trends are preserved across different values of the dimensionless heat of reaction *B*, confirming the structural nature of the identified regimes.

A first relevant observation from Figs. 8 and 9 is the absence of a second cold-spot operation regime (CSO_2) within the investigated operating domain. This behaviour is consistent with the equilibrium-limited nature of the rWGS reaction, for which conversion and yield progressively approach their asymptotic values without exhibiting an internal maximum under the conditions considered. Consequently, only the first cold-spot operation regime (CSO_1) is identified and is hereafter simply referred to as cold-spot operation (CSO).

Under the investigated operating conditions and imposed-current heating formulation, no SENS-type operating regions were observed for the present reactor configuration. This behaviour is consistent with the predominance of the strongly endothermic rWGS thermal response and the absence of significant positive thermal feedback mechanisms within the explored operating domain. Moreover, the comparatively weak temperature dependence of the FeCrAl electrical resistivity limits electrothermal coupling effects under the adopted Joule-heating formulation. Accordingly, the absence of SENS-type behaviour should be interpreted as specific to the investigated reactor configuration, chemistry, heating mode, and operating conditions considered in the present work.

Focusing on the regimes identified in Fig. 8, corresponding to the design-oriented operating-regime map, the HTO region is not encountered within the investigated design domain. This result indicates that the selected reactor configuration operates with substantial separation from thermally inadmissible conditions associated with catalyst and reactor-material temperature constraints. In contrast, the no-flow (NF) regime reflects operating conditions for which the inlet pressure becomes insufficient to overcome frictional losses and sustain flow through the reactor. This regime has received limited attention in previous stability studies because it originates from hydrodynamic constraints rather than thermo-kinetic phenomena. For the present configuration, the nominal operating point remains well separated from the NF region, indicating adequate operability margins with respect to flow-related limitations.

At low Damköhler numbers, transitions between cold-spot operation (CSO) and pseudo-adiabatic operation (PAO) are observed. This behaviour is related to the cumulative balance between endothermic heat absorption and distributed Joule heating along the reactor length. Short-contact-time configurations are characterized by limited reaction extent and reduced cumulative endothermic cooling, such that the temperature profile generally remains monotonic and PAO behaviour is observed. Conversely, longer contact times increase the cumulative heat absorbed by the endothermic reaction, promoting the formation of an internal axial temperature minimum and therefore CSO behaviour.

Along the investigated *Da*–*B* domain, operating points within the CSO region are generally associated with higher conversion and yield than those located in the PAO region, reflecting the greater overall reaction extent achieved at longer contact times. Under the selected operating conditions, the reference reactor operates within the CSO regime and remains well separated from the HTO, NF, and PAO boundaries. The longer residence times associated with CSO operation also favour downstream CH_4 consumption, leading to progressively lower CH_4 concentrations toward the reactor outlet.

Control implications are illustrated in Fig. 9, which maps how inlet disturbances may drive regime transitions at fixed reactor geometry. The dominant risk is the transition from cold-spot operation (CSO) to high-temperature operation (HTO), corresponding to inlet-to-outlet overheating when electrical heating is held constant. In this regime, active adjustment of the heat input is required to remain within admissible temperature limits.

Approaching the HTO–CSO boundary, outlet temperatures increase markedly, while operating conditions within the HTO region are characterized by progressively higher reactor temperatures. Under these conditions, the imposed thermal input exceeds the compensating effect of endothermic heat absorption, leading to monotonic temperature increases along the reactor length. Consequently, these operating conditions may exceed catalyst and reactor-material temperature limits and are therefore considered thermally inadmissible. These transitions occur primarily at low Damköhler numbers, where reduced conversion lowers the endothermic heat sink and favours thermal accumulation. Higher values of the dimensionless heat parameter *B* further aggravate this behaviour by increasing the thermal burden and promoting CH_4 formation, with a detrimental impact on selectivity.

Figs. 8 and 9 provide complementary operating envelopes for design validation and control. Fig. 8 quantifies how reactor geometry and geometrical degrees of freedom shape regimes and performance, whereas Fig. 9 links inlet disturbances to regime transitions and can be embedded in model-based control/diagnostic frameworks to prevent entry into hot-spot operation—particularly valuable for emerging Joule-heated wall reactor technology.

5.4. Inlet disturbances and intensification limits

To further illustrate the usefulness of stability diagrams for control and process intensification, variations in inlet conditions are superimposed onto the stability map, generating trajectories that describe the evolution of the reactor operating point. This representation explicitly links operational changes to regime transitions and performance trends, as shown in Fig. 10, where dimensional inlet variations are embedded within the dimensionless stability framework.

Variations in inlet conditions—specifically the inlet molar flow rate $\dot{n}_{in,tube}$ and inlet temperature T_{in}—can be directly interpreted as shifts in the dimensionless numbers *Da* and *B*. Since the stability diagram is constructed from a parametric sensitivity analysis of the governing dimensionless groups, the influence of inlet conditions is inherently captured. The introduction of operating trajectories makes this dependency explicit, enabling visualization of how the reactor operating point moves within the stability space and how this motion correlates with changes in regime, performance, and operability margins. This provides a compact, physics-based tool to assess operability and to explore intensified operating conditions.

For the present case study, the nominal inlet molar flow rate ($\dot{n}_{in,tube} = 0.1\ kmol\ h^{-1}$) is perturbed by ±80%, while the inlet temperature ($T_{in} = 750\ ^{\circ}C$) is varied by $\pm\ 200\ ^{\circ}C$. A decrease in $\dot{n}_{in,tube}$ may represent malfunctions in the upstream feeding system, whereas an increase reflects throughput-driven intensification strategies. For $\dot{n}_{in,tube} > 0.18\ kmol\ h^{-1}$, fluid flow cannot be sustained because the resulting pressure drop exceeds the available driving pressure, requiring a higher inlet pressure. As the inlet flow rate increases, the operating point moves closer to the HTO–CSO transition boundary. Although this boundary is not crossed under the investigated conditions, the progressive approach toward the HTO region highlights the trade-offs between throughput, conversion efficiency, and thermal constraints. In this regard, the operating-regime maps provide a quantitative framework for assessing operability margins and evaluating the effects of throughput intensification on reactor performance and thermal behaviour.

Inlet temperature variations affect both *Da* and *B*, with a dominant

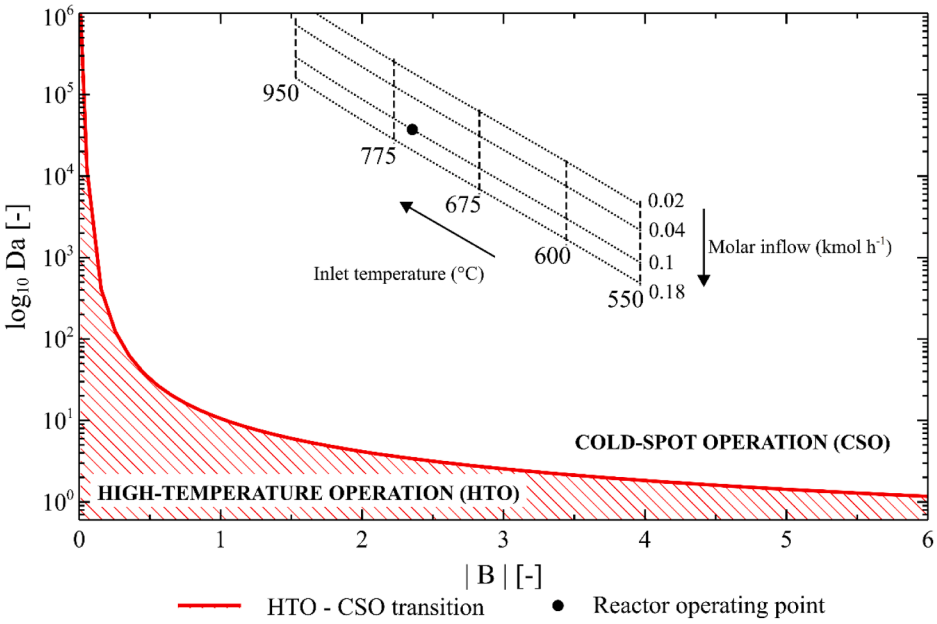

Fig. 10. Operating-regime diagrams augmented with representative operating-point trajectories associated with variations in dimensional inlet conditions. The horizontal axis reports the absolute value |B| of the dimensionless thermal parameter for consistency with the canonical VMWT graphical representation.

impact on *Da* due to the temperature dependence of reaction kinetics. Increasing T_{in} shifts the operating point toward higher reaction rates and enhanced heat absorption, increasing the thermal-operability margin relative to the HTO boundary. This suggests that moderate feed preheating can be exploited as an effective intensification lever. Conversely, reduced inlet temperatures diminish the endothermic heat sink and push the operating point toward the instability boundary, an effect analogous to that induced by increasing inlet flow rate and potentially arising from upstream heating failures or control disturbances.

Although the present analysis is based on steady-state operating-regime maps, the resulting framework may also provide useful qualitative insight into how reactor operating conditions evolve during changes in process inputs. For example, variations in inlet temperature, flow rate, or electrical-heating intensity can be interpreted as trajectories across the operating-regime maps, thereby relating operating-condition changes to the corresponding regime boundaries and operability margins.

From this perspective, the proposed framework may support interpretation of operating-condition changes and assessment of their potential impact on reactor performance and thermal behaviour. More generally, this trajectory-based representation illustrates the potential applicability of the approach to electrified reactor systems operating under variable process and power-supply conditions, beyond the specific rWGS case study considered here.

6. Conclusions

A sensitivity-based modelling and operability-assessment framework for Joule-heated multitubular fixed-bed reactors has been developed and applied to the reverse water–gas shift (rWGS) reaction using complementary one- and two-dimensional formulations. The adopted kinetic model was selected through comparative assessment of literature formulations under electrified operating conditions. The close agreement between the one- and two-dimensional models indicates limited radial transport effects within the investigated operating domain, supporting the use of simplified one-dimensional descriptions for design and operability analyses. Both formulations consistently predict the formation of an inlet cold spot, confirming its role as a characteristic feature of the investigated reactor configuration.

Beyond reactor modelling, this work extends the application of the VMWT framework to electrified endothermic reactors and demonstrates how operating-regime maps can be used to identify regime transitions, operability limits, and performance trends. Within this perspective, cold-spot behaviour emerges as a characteristic steady-state operating regime rather than as a numerical artifact or geometry-specific feature.

For Joule-heated operation, electrical current provides an effective means of regulating reactor thermal behaviour. Increasing current enhances downstream temperature recovery and conversion, whereas the inlet cold spot remains comparatively weakly affected because its formation is governed primarily by the strong endothermic heat demand near the reactor inlet.

The analysis further indicates that long-contact-time operation within the CSO regime provides favourable performance–operability trade-offs, promoting higher conversion while maintaining thermally admissible operation. Conversely, short-contact-time configurations tend to operate in the PAO regime, where reduced cumulative endothermic cooling prevents the formation of an internal temperature minimum.

The transition between PAO and CSO regimes is governed by the balance between cumulative endothermic heat absorption and the distributed thermal input provided by Joule heating along the reactor length. The proposed framework therefore establishes a direct connection between reactor contact time, thermal-profile evolution, and operating-regime transitions in electrified endothermic reactors.

Overall, the proposed operability and performance maps are shown to provide a priori support for reactor design and operability assessment rather than ex-post diagnostic analysis. The framework enables systematic identification of operating envelopes, regime-transition boundaries, and operability margins without relying exclusively on extensive case-specific parametric studies. In this way, it establishes a direct link between reactor design, operating conditions, and thermal behaviour in electrified endothermic reactors. For the investigated reactor configuration, the nominal operating point remains well separated from the HTO region throughout the investigated operating range, indicating appreciable thermal-operability margins.

Future work may extend the analysis to transient operation, including startup, shutdown, and load-following conditions under variable electrical-power input, while accounting for axial wall-conduction effects.

CRediT authorship contribution statement

Giuseppe Andriani: Writing – original draft, Methodology, Investigation, Formal analysis, Data curation. **Paolo Mocellin:** Writing – review & editing, Supervision, Resources, Project administration, Methodology, Funding acquisition, Conceptualization. **Gianmaria Pio:** Writing – review & editing, Visualization, Validation, Methodology. **Ernesto Salzano:** Writing – review & editing, Supervision, Project administration, Methodology. **Chiara Vianello:** Writing – review & editing, Visualization, Software, Resources.

Declaration of competing interest

The authors declare that they have no known competing financial interests or personal relationships that could have appeared to influence the work reported in this paper.

Supplementary material

Supplementary material associated with this article can be found, in the online version, at doi:10.1016/j.cep.2026.110960.

Data availability

Data will be made available on request.

References

[1] G. Andriani, G. Pio, C. Vianello, P. Mocellin, E. Salzano, Safety parameters and stability diagram of hydroxylamine hydrochloride and sulphate, Chem. Eng. J. 482 (Feb. 2024), https://doi.org/10.1016/j.cej.2024.148894.

[2] G. Andriani, G. Pio, E. Salzano, C. Vianello, P. Mocellin, Evaluating the thermal stability of chemicals and systems: a review, Can. J. Chem. Eng. (2024), https://doi.org/10.1002/cjce.25422.

[3] G. Andriani, P. Mocellin, G. Pio, C. Vianello, E. Salzano, Enhancing safety in the storage of hazardous molecules: the case of hydroxylamine, J. Loss Prev. Process Ind. 92 (Dec. 2024), https://doi.org/10.1016/j.jlp.2024.105472.

[4] G. Andriani, B.A. De Liso, G. Pio, E. Salzano, Design of sustainable reactor based on key performance indicators, Chem. Eng. Sci. 285 (Mar. 2024), https://doi.org/10.1016/j.ces.2023.119591.

[5] A. Varma, M. Morbidelli, H. Wu, Parametric Sensitivity in Chemical Systems, 1st ed., Cambridge University Press, 1999.

[6] K.R. Westerterp, E.J. Molga, Safety and runaway prevention in batch and semibatch reactors - a review, Chem. Eng. Res. Des. 84 (7 A) (2006) 543–552, https://doi.org/10.1205/cherd.05221.

[7] J. Zhang, C.J. Tighe, K. Hellgardt, D. Unruh, R. Bos, Generalized runaway diagrams for catalytic reactors with stacked catalyst activities, Chem. Eng. J. 502 (2024), https://doi.org/10.1016/j.cej.2024.157960.

[8] G. Andriani, P. Mocellin, G. Pio, E. Salzano, C. Vianello, Design of storage equipment for unstable chemicals using sensitivity-based methods, Ind. Eng. Chem. Res. (2025), https://doi.org/10.1021/acs.iecr.5c00127.

[9] M. Zanfir, A. Gavriilidis, Catalytic combustion assisted methane steam reforming in a catalytic plate reactor, Chem. Eng. Sci. 58 (17) (2003) 3947–3960, https://doi.org/10.1016/S0009-2509(03)00279-3.

[10] F. Wang, G. Wang, Performance and cold spot effect of methanol steam reforming for hydrogen production in micro-reactor, Int. J. Hydrog. Energy 41 (38) (Oct. 2016) 16835–16841, https://doi.org/10.1016/j.ijhydene.2016.07.083.

[11] G.F. Froment, K.B. Bischoff, J. De Wilde, Chemical Reactor Analysis and Design, 3rd ed., John Wiley & Sons, Inc., 2011.

[12] M. Zanfir and A. Gavriilidis, "Parametric sensitivity in catalytic plate reactors with first-order endothermic-exothermic reactions," 2002.

[13] M. Bayat, M.R. Rahimpour, M. Taheri, M. Pashaei, S. Sharifzadeh, A comparative study of two different configurations for exothermic-endothermic heat exchanger reactor, Chem. Eng. Process.: Process Intensif. 52 (2012) 63–73, https://doi.org/10.1016/j.cep.2011.11.010.

[14] G. Andriani, L. Salano, M. Maria Bozzini, P. Mocellin, F. Manenti, C. Vianello, Sustainability-oriented process optimization for biogas to methanol: balancing safety, economics, and environmental parameters, Ind. Eng. Chem. Res. (2025), https://doi.org/10.1021/acs.iecr.5c00494.

[15] V. L. Gole and P. R. Gogate, "A review on intensification of synthesis of biodiesel from sustainable feed stock using sonochemical reactors," 2012. doi: 10.1016/j.cep.2011.12.008.

[16] L. Zheng, M. Ambrosetti, A. Beretta, G. Groppi, E. Tronconi, Electrified CO2 valorization driven by direct joule heating of catalytic cellular substrates, Chem. Eng. J. 466 (2023), https://doi.org/10.1016/j.cej.2023.143154.

[17] G. Cao, R.M. Handler, W.L. Luyben, Y. Xiao, C.H. Chen, J. Baltrusaitis, CO2 conversion to syngas via electrification of endothermal reactors: process design and environmental impact analysis, Energy Convers. Manag. 265 (Aug. 2022), https://doi.org/10.1016/j.enconman.2022.115763.

[18] L. Zheng, M. Ambrosetti, E. Tronconi, Joule-heated catalytic reactors toward decarbonization and process intensification: a review, ACS Eng. Au (2023), https://doi.org/10.1021/acsengineeringau.3c00045.

[19] Y.T. Kim, J.J. Lee, J. Lee, Electricity-Driven Reactors that Promote Thermochemical Catalytic Reactions Via Joule and Induction Heating, Elsevier B. V., 2023, https://doi.org/10.1016/j.cej.2023.144333.

[20] R. Mallada, The central role of materials in heterogeneous catalytic intensified processes, Chem. Eng. Process. - Process Intensif. 221 (2026) 110691, https://doi.org/10.1016/j.cep.2025.110691.

[21] J.G. Segovia-Hernández, Process intensification for e-waste valorization: economic & energy advantages over conventional recovery routes, Chem. Eng. Process. - Process Intensif. 221 (2026) 110708, https://doi.org/10.1016/j.cep.2026.110708.

[22] R.R. Ratnakar, V. Balakotaiah, Sensitivity analysis of hydrogen production by methane reforming using electrified wire reactors, Int. J. Hydrog. Energy 49 (2024) 916–926, https://doi.org/10.1016/j.ijhydene.2023.07.352.

[23] M. Ambrosetti, A perspective on power-to-heat in catalytic processes for decarbonization, Chem. Eng. Process. - Process Intensif. 182 (Dec. 2022), https://doi.org/10.1016/j.cep.2022.109187.

[24] F. Cameli, M. Scapinello, E. Delikonstantis, G.D. Stefanidis, Electrified methane upgrading via non-thermal plasma: intensified single-pass ethylene yield through structured bimetallic catalyst, Chem. Eng. Process. - Process Intensif. 204 (2024), https://doi.org/10.1016/j.cep.2024.109946.

[25] V. Tomašić, Z. Gomzi, Experimental and theoretical study of NO decomposition in a catalytic monolith reactor, Chem. Eng. Process.: Process Intensif. 43 (6) (2004) 765–774, https://doi.org/10.1016/S0255-2701(03)00045-X.

[26] B. Tidona, A. Urakawa, P. Rudolf von Rohr, High pressure plant for heterogeneous catalytic CO2 hydrogenation reactions in a continuous flow microreactor, Chem. Eng. Process.: Process Intensif. 65 (2013) 53–57, https://doi.org/10.1016/j.cep.2013.01.001.

[27] Y.A. Daza, J.N. Kuhn, CO2 conversion by reverse water gas shift catalysis: comparison of catalysts, mechanisms and their consequences for CO2 conversion to liquid fuels, RSC Adv. 6 (55) (2016) 49675–49691, https://doi.org/10.1039/C6RA05414E.

[28] A. Mion, F. Galli, P. Mocellin, S. Guffanti, G. Pauletto, Electrified methane reforming decarbonises methanol synthesis, J. CO2 Util. 58 (2022), https://doi.org/10.1016/j.jcou.2022.101911.

[29] G. Pauletto, F. Galli, A. Gaillardet, P. Mocellin, G.S. Patience, Techno economic analysis of a micro gas-to-liquid unit for associated natural gas conversion, Renew. Sustain. Energy Rev. 150 (2021), https://doi.org/10.1016/j.rser.2021.111457.

[30] M.F. Santos, A.E. Bresciani, N.L. Ferreira, G.S. Bassani, R.M.B. Alves, Carbon dioxide conversion via reverse water-gas shift reaction: reactor design, J. Env. Manage 345 (2023), https://doi.org/10.1016/j.jenvman.2023.118822.

[31] M.M. Tijani, E. Mostafavi, N. Mahinpey, Process simulation and thermodynamic analysis of a chemical looping combustion system using methane as fuel and NiO as the oxygen carrier in a moving-bed reactor, Chem. Eng. Process. - Process Intensif. 144 (2019), https://doi.org/10.1016/j.cep.2019.107636.

[32] A. Wolf, A. Jess, C. Kern, Syngas production via reverse water-gas shift reaction over a Ni-Al2O3 catalyst: catalyst stability, reaction kinetics, and modeling, Chem. Eng. Technol. 39 (6) (Jun. 2016) 1040–1048, https://doi.org/10.1002/ceat.201500548.

[33] J.A. Loiland, M.J. Wulfers, N.S. Marinkovic, R.F. Lobo, Fe/γ-Al2O3 and Fe-K/γ-Al2O3 as reverse water-gas shift catalysts, Catal. Sci. Technol. 6 (14) (2016) 5267–5279, https://doi.org/10.1039/c5cy02111a.

[34] C.Y. Chou, J.A. Loiland, R.F. Lobo, Reverse water-gas shift iron catalyst derived from magnetite, Catalysts 9 (9) (Sep. 2019), https://doi.org/10.3390/catal9090773.

[35] M.J.L. Ginés, A.J. Marchi, C.R. Apesteguía, Kinetic study of the reverse water-gas shift reaction over CuO/ZnO/A1203 catalysts, Appl. Catal. Gen. 154 (1997) 155–171, https://doi.org/10.1016/S0926-860X(96)00369-9.

[36] N.A. Koryabkina, A.A. Phatak, W.F. Ruettinger, R.J. Farrauto, F.H. Ribeiro, Determination of kinetic parameters for the water-gas shift reaction on copper catalysts under realistic conditions for fuel cell applications, J. Catal. 217 (1) (Jul. 2003) 233–239, https://doi.org/10.1016/S0021-9517(03)00050-2.

[37] K.-H. Ernst, C.T. Campbell, G. Moretti', Kinetics of the reverse water-gas shift reaction over Cu(110), J. Catal 134 (1992) 66–74, https://doi.org/10.1016/0021-9517(92)90210-9.

[38] G. Ertl, H. Knozinger, F. Schuth, J. Weitkamp, Handbook of Heterogeneous Catalysis, 2nd ed., Wiley-VCH, 2008.

[39] E. Pahija, et al., Experimental and Computational Synergistic Design of Cu and Fe Catalysts for the Reverse Water-Gas Shift: A Review, American Chemical Society, 2022, https://doi.org/10.1021/acscatal.2c01099.

[40] O.Y. Boakye, S.M. Hashemi, N. Mahinpey, Investigation of Al2O3, ZrO2, SiO2, and CeO2 supported nickel catalysts for tri-reforming of methane, Int. J. Hydrog. Energy 109 (2025) 802–812, https://doi.org/10.1016/j.ijhydene.2025.02.098.

[41] C.A.H. Price, E. Earles, L. Pastor-Pérez, J. Liu, T.R. Reina, Advantages of yolk shell catalysts for the DRM: A comparison of Ni/ZnO@SiO2 vs. Ni/CeO2 and Ni/Al2O3, Chemistry (Switzerland) 1 (1) (Dec. 2019) 3–16, https://doi.org/10.3390/chemistry1010003.

[42] J.A. Hernandez Lalinde, P. Roongruangsree, J. Ilsemann, M. Bäumer, J. Kopyscinski, CO2 methanation and reverse water gas shift reaction. Kinetic study based on in situ spatially-resolved measurements, Chem. Eng. J. 390 (Jun. 2020), https://doi.org/10.1016/j.cej.2020.124629.

[43] J.A. Moulijn, M. Makkee, A.E. Van Diepen, Chemical Process Technology, 2nd ed., John Wiley & Sons, 2013.

[44] J. Xu, G.F. Froment, Methane steam reforming, methanation and water-gas shift: 1. Intrinsic kinetics, AIChE J. 35 (1) (1989) 88–96, https://doi.org/10.1002/aic.690350109.
[45] K. Hou, R. Hughes, The kinetics of methane steam reforming over a Ni/-Al2O3 catalyst, Chem. Eng. J. 82 (1–3) (2001) 311–328, https://doi.org/10.1016/S1385-8947(00)00367-3.
[46] F. Vidal Vázquez, P. Pfeifer, J. Lehtonen, P. Piermartini, P. Simell, V. Alopaeus, Catalyst screening and kinetic modeling for CO production by high pressure and temperature reverse water gas shift for Fischer-Tropsch applications, Ind. Eng. Chem. Res. 56 (45) (Nov. 2017) 13262–13272, https://doi.org/10.1021/acs.iecr.7b01606.
[47] A. Cybulski, J.A. Moulijn, Structured Catalysts and Reactors, 2nd ed., CRC Press, 2006.
[48] S. Govender, H.B. Friedrich, Monoliths: A Review of the Basics, Preparation Methods and Their Relevance to Oxidation, MDPI, 2017, https://doi.org/10.3390/catal7020062.
[49] T. Nonnast, BASF, SABIC, and Linde celebrate the start-up of the world's first large-scale electrically heated steam cracking furnace, Accessed: Jul. 19, 2024. [Online]. Available: https://www.basf.com/global/en/media/news-releases/2024/04/p-24-177.html, 2024.
[50] S.T. Wismann, et al., Electrified methane reforming: a compact approach to greener industrial hydrogen production, Science (1979) 364 (6442) (2019) 756–759, https://doi.org/10.1126/science.aaw8775.
[51] O. Levenspiel, Chemical Reaction Engineering, 3rd ed., John Wiley & Sons, 1999.
[52] H.S. Fogler, Elements of Chemical Reaction Engineering, 6th ed., Pearson, 2020.
[53] G. Bozga, A.V. Brosteanu, I. Banu, A.C. Dimian, One-stage ethanol to butadiene process: analysis and design of a multi-tubular fixed bed reactor, Chem. Eng. Res. Des. 203 (Mar. 2024) 608–618, https://doi.org/10.1016/j.cherd.2024.01.070.
[54] H.A. Jakobsen, Chemical Reactor Technology : Multiphase Reactive Computational Fluid Dynamics, 1st ed., Springer, 2008.
[55] A. Mostafa, A. Beretta, G. Groppi, E. Tronconi, M.C. Romano, A novel electrified sorption enhanced reforming process for blue hydrogen production, Energy Adv. 4 (5) (Mar. 2025) 624–638, https://doi.org/10.1039/d4ya00540f.
[56] H.H. Koybasi, D. Liu, D.G. Vlachos, Computational insights into an electrified, washcoated nonoxidative propane dehydrogenation reactor, Ind. Eng. Chem. Res. 64 (24) (2025) 11804–11814, https://doi.org/10.1021/acs.iecr.5c00980.
[57] K. Barati, Y. Khojasteh-Salkuyeh, Development and analysis of electrified combined reforming of methane and CO2 based on induction and resistance heating, Energy Convers. Manag 347 (2026), https://doi.org/10.1016/j.enconman.2025.120585.
[58] A. Rupnik, I. Shlyapnikov, M. Grilc, G. Veryasov, D. Bajec, B. Likozar, A Review of Electrified Methane Conversion: Utilizing Electrocatalysis, Plasma, Electric-Field and Electro-Thermal Technologies, John Wiley and Sons Inc, 2025, https://doi.org/10.1002/tcr.202400256.
[59] T.O. Salmi, J.-P. Mikkola, J.P. Wärnå, Chem. React. Eng. React. Technol. (2018).
[60] J. Knochen, R. Güttel, C. Knobloch, T. Turek, Fischer-Tropsch synthesis in milli-structured fixed-bed reactors: experimental study and scale-up considerations, Chem. Eng. Process.: Process Intensif. 49 (9) (Sep. 2010) 958–964, https://doi.org/10.1016/j.cep.2010.04.013.
[61] G. Ferri, M. Ambrosetti, A. Beretta, G. Groppi, E. Tronconi, Experimental investigation and 2D mathematical modelling of copper foams packed with Rh-Al2O3 catalysts for the intensification of methane steam reforming, Catal. Today 426 (Jan. 2024), https://doi.org/10.1016/j.cattod.2023.114386.
[62] S. Hiroyasu, R. Watanabe, P. Verma, H. Akama, C. Fukuhara, Integrated electrified reactor system for efficient CO2-to-syngas conversion via e-methanation and e-POM, React. Chem. Eng. (Sep. 2025), https://doi.org/10.1039/d5re00196j.
[63] L. Vergani, M. Ambrosetti, G. Groppi, Electrified dehydrogenation of methyl-cyclohexane: reactor modeling and process integration, Chem. Eng. Process. - Process Intensif. 215 (Sep. 2025), https://doi.org/10.1016/j.cep.2025.110368.
[64] H. Asmat, et al., Electrified reformer for syngas production – additive manufacturing of coated microchannel monolithic reactor, Appl. Catal. B 361 (Feb. 2025), https://doi.org/10.1016/j.apcatb.2024.124640.
[65] M. Morbidelli, A. Varma, A generalized criterion for parametric sensitivity: application to a pseudohomogeneous tubular reactor with consecutive or parallel reactions, Chem. Eng. Sci. 44 (8) (1989) 1675–1696, https://doi.org/10.1016/0009-2509(89)80010-7.
[66] M. Morbidelli, A. Varma, A generalized criterion for parametric sensitivity: application to thermal explosion theory, Chem. Eng. Sci. 43 (I) (1988) 9–102, https://doi.org/10.1016/0009-2509(88)87129-X.
[67] M. Morbidelli, A. Vat-Ma, Parametric sensitivity and runaway in fixed-bed catalytic reactors, Chem. Eng. Sci. 41 (4) (1986) 1063–1071, https://doi.org/10.1016/0009-2509(86)87193-7.
[68] V. Balakotaiah, S.M.S. Dommeti, N. Gupta, Bifurcation analysis of chemical reactors and reacting flows, Chaos 9 (1) (1999) 13–35, https://doi.org/10.1063/1.166377.
[69] S.I. Sandler, Chemical, Biochemical, and Engineering Thermodynamics, 5th ed., Wiley, 2017.
[70] K.R. Westerterp, E.J. Molga, No more runaways in fine chemical reactors, Ind. Eng. Chem. Res. 43 (16) (Aug. 2004) 4585–4594, https://doi.org/10.1021/ie030725m.
[71] G. Andriani, G. Pio, C. Vianello, P. Mocellin, E. Salzano, Electrical conductivity as an indicator for early warning detection systems in chemical reactors, J. Electrostat. 138 (Dec. 2025), https://doi.org/10.1016/j.elstat.2025.104154.
[72] V. Balakotaiah, On the steady-state behaviour of the autocatalator model A + 2B⇌3B, B⇌C in a continuous-flow stirred-tank reactor, in: Proceedings of the Royal Society of London. A. Mathematical and Physical Sciences 411, May 1987, pp. 193–206, https://doi.org/10.1098/rspa.1987.0061.
[73] D.E. Seborg, T.F. Edgar, D.A. Mellichamp, F.J.I. Doyle, Process Dynamics and Control, 4th ed., Wiley, 2019.
[74] A.M. Flynn, T. Akashige, L. Theodore, Kern's Process Heat Transfer, 2nd ed., Wiley, 2019.
[75] S.T. Wismann, et al., Electrified methane reforming: elucidating transient phenomena, Chem. Eng. J. 425 (Dec. 2021), https://doi.org/10.1016/j.cej.2021.131509.
[76] M.V. Twigg, Catalyst Handbook, 2nd ed., Wlfe Publishing, 1989.
[77] J. Zhu, X. Cui, S.S. Araya, Comparison between 1D and 2D numerical models of a multi-tubular packed-bed reactor for methanol steam reforming, Int. J. Hydrog. Energy 47 (54) (Jun. 2022) 22704–22719, https://doi.org/10.1016/j.ijhydene.2022.05.109.
[78] D. Luss, V.W. Weekman Jr., Chemical Reaction Engineering Reviews - ACS Symposium Series, American Chemical Society, 1978.
[79] J.F. Richardson, J.H. Harker, J.R. Backhurst, Coulson and Richardson's - Chemical Engineering, 6th ed., 6, Elsevier, 2020.
[80] D.-M. Liu, W.H. Tuan, C.-C. Chiu, Thermal diffusivity, heat capacity and thermal conductivity in Al203-Ni composite, Mater. Sci. Eng.: B 31 (3) (1995) 287–291, https://doi.org/10.1016/0921-5107(94)01163-X.
[81] X. Zhou, C. Chen, F. Wang, Modeling of non-catalytic partial oxidation of natural gas under conditions found in industrial reformers, Chem. Eng. Process.: Process Intensif. 49 (1) (2010) 59–64, https://doi.org/10.1016/j.ijhydene.2009.12.063.
[82] E. Turan, et al., Direct resistive heating of a catalytic fixed-bed reactor for ethanol dehydration, Chem. Eng. J. 514 (Jun. 2025), https://doi.org/10.1016/j.cej.2025.162963.
[83] G.F. Froment, K.B. Bischoff, J. De Wilde, Chemical Reactor Analysis and Design, 3rd ed., John Wiley & Sons, 2011.
[84] L.E. Basini, F. Furesi, M. Baumgärtl, N. Mondelli, G. Pauletto, CO2 capture and utilization (CCU) by integrating water electrolysis, electrified reverse water gas shift (E-RWGS) and methanol synthesis, J. Clean. Prod. 377 (Dec. 2022), https://doi.org/10.1016/j.jclepro.2022.134280.
[85] X. Liang, W. Xu, C.Y. Chung, W. Freitas, K. Xiong, Dynamic load models for industrial facilities, IEEE Trans. Power Syst. 27 (1) (Feb. 2012) 69–80, https://doi.org/10.1109/TPWRS.2011.2161781.
[86] R. Alves, P. Neves, D. Gonçalves, J.G. Pinto, J. Batista, J.L. Afonso, Electric Power Quality Monitoring Results in Different Facilities, IEEE, 2009, https://doi.org/10.1109/IECON.2009.5415137.
[87] H. Karibe, S. Sair, A. Faik, H.Ait Ousaleh, Electrified Steam Methane Reforming: A Review of Heating Technologies, Challenges, and Prospects, Elsevier Ltd, 2025, https://doi.org/10.1016/j.ijhydene.2025.04.475.
[88] M. Baldea, et al., Transforming the process industries through electrification: challenges and opportunities, Ind. Eng. Chem. Res (Aug. 2025), https://doi.org/10.1021/acs.iecr.5c01256.
[89] K. G. Field, M. A. Snead, Y. Yamamoto, and K. A. Terrani, "Handbook on the material properties of FeCrAl alloys for nuclear power production applications," 2017.
[90] G. Pauletto, et al., FeCrAl as a catalyst support, Chem. Rev. 120 (15) (Aug. 2020) 7516–7550, https://doi.org/10.1021/acs.chemrev.0c00149.
[91] D.W. Green, M.Z. Southard, Perry's Chemical Engineers' Handbook, 9th ed., McGraw-Hill Education, 2019.
[92] J. Barrientos, N. González, M. Lualdi, M. Boutonnet, S. Järås, The effect of catalyst pellet size on nickel carbonyl-induced particle sintering under low temperature CO methanation, Appl. Catal. A Gen. 514 (Mar. 2016) 91–102, https://doi.org/10.1016/j.apcata.2015.12.034.